A brief history of Wavefront Sensors

François Hénault
Institut de Planétologie et d'Astrophysique de Grenoble
Université Grenoble-Alpes
Centre National de la Recherche Scientifique
BP 53, 38041 Grenoble – France

Abstract

- Wavefront sensors (WFS) are widespread in the field of optical measurements. Originally conceived more than 40 years ago for adaptive optics (AO) systems in astronomy, they are now key elements in biomedical applications, metrology of optical components, and characterization of laser beams. Some of the most popular WFS are the Shack–Hartmann based on a micro-lens array placed at the pupil of the optical system and the pyramidal sensor that combines four pupil images seen through a small pyramid prism located at the focus of the system.

- After a brief introduction about the of wavefront sensing and AO, we will review the main types of existing WFS (not only the two listed above) and their operating principle in open loop. The talk will then be focused at three new potential developments:
  - New WFS family based on the Ronchi or reverse Hartmann tests: System optimization and achievable measurement accuracy
  - How to use your WFS from behind a coronagraph phase mask ?
  - A “solar” wavefront sensor usable to characterizing the shape and alignment errors of solar concentrators, by means of a “backward gazing” method

Plan

- Basics of adaptive optics and wavefront sensing
  - Main types of wavefront sensors
- A Ronchi-Reverse Hartmann wavefront sensor
- Operating from behind a coronagraph mask
- A “backward gazing” solar wavefront sensor
- Conclusion

Adaptive optics and wavefront sensing

- Examples
- Generalities
- Elementary optical relations
- Main types of wavefront sensors
  - Shack-Hartmann
  - Curvature sensor
  - Optical differentiation sensor
  - Pyramidal wavefront sensor
  - Zernike wavefront sensor (Zelda)

Adaptive Optics: application to astronomy

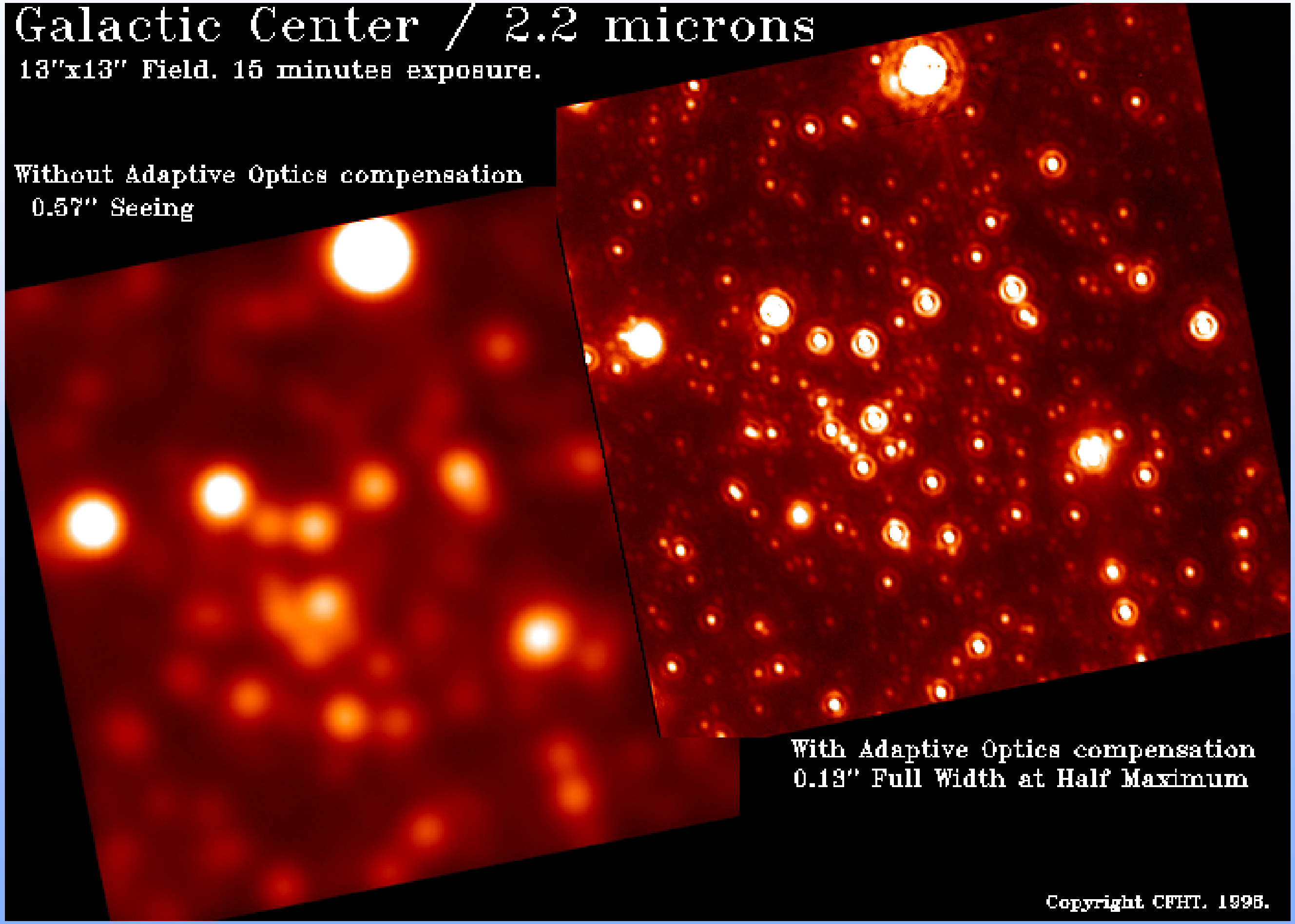

- **Galactic center, 15 minutes exposure time, CFHT (∅ 3,6 m)**

Adaptive Optics: application to astronomy

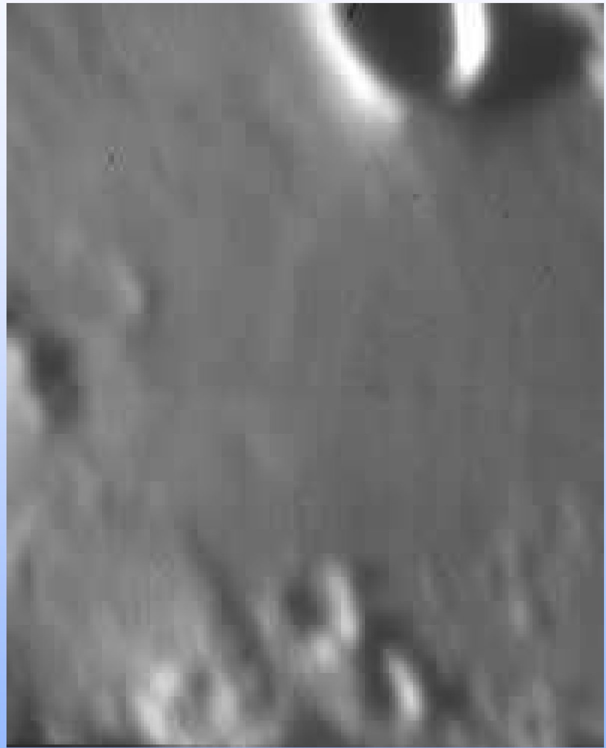

- Image of the Moon with AO system NAOS with VLT (∅ 8 m), K band (2.3 µm)

Future ELTs (Extremely Large Telescopes)

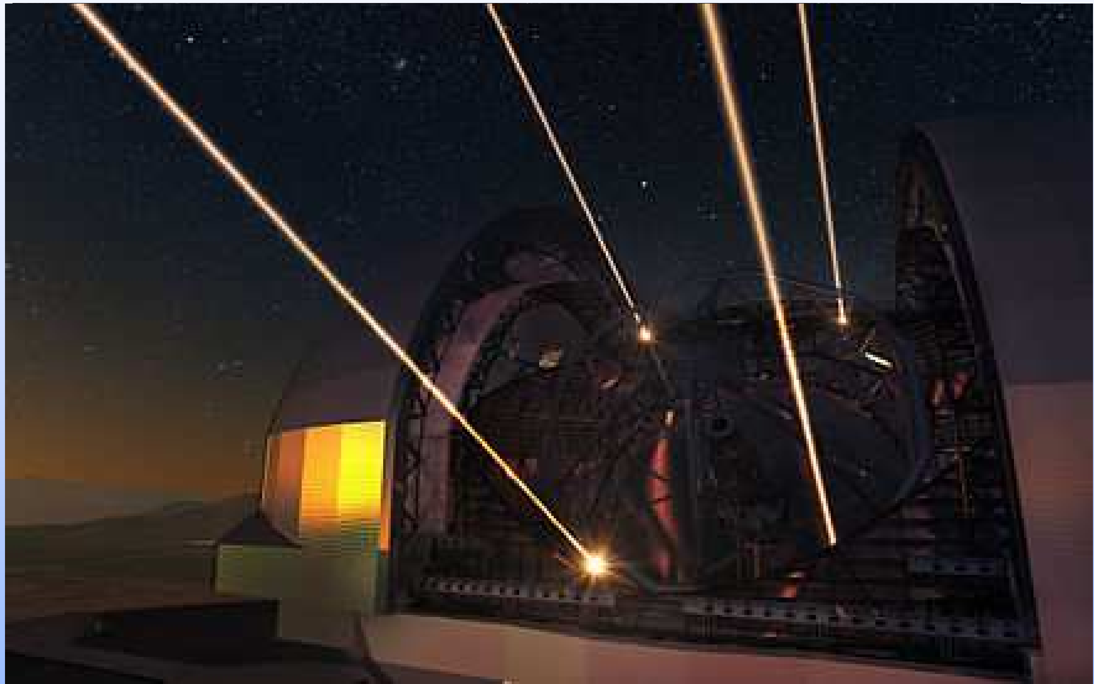

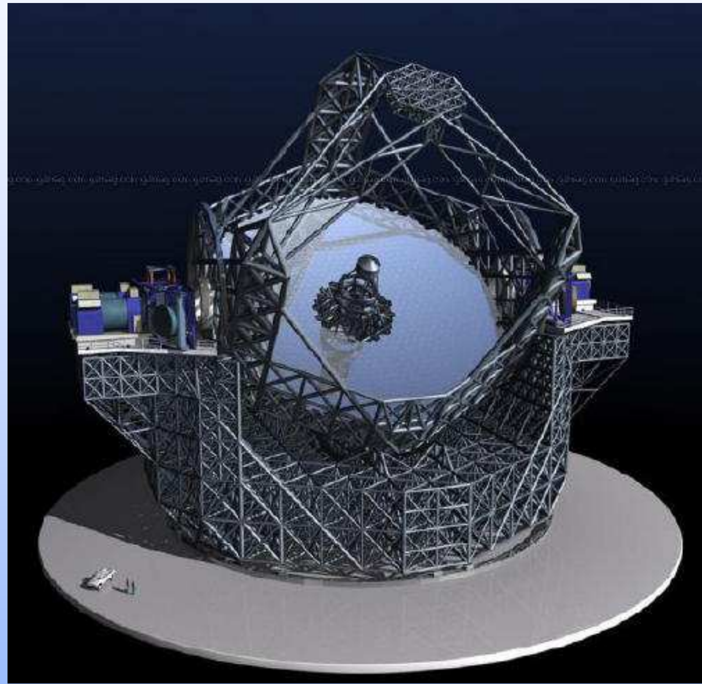

- American and European projects (Thirty Meter Telescope ∅ 30 m, E-ELT ∅ 39 m), first lights in 2024-2025
- Unprecedented challenge for AO and wavefront sensors, especially in presence of Laser guide stats (LGS)

Active and Adaptive Optics

- Active optics
  - **Open loop** operation
  - Refresh rate ≈ a few minutes
  - Correction applied to the distorted mirror
  - No additional optics

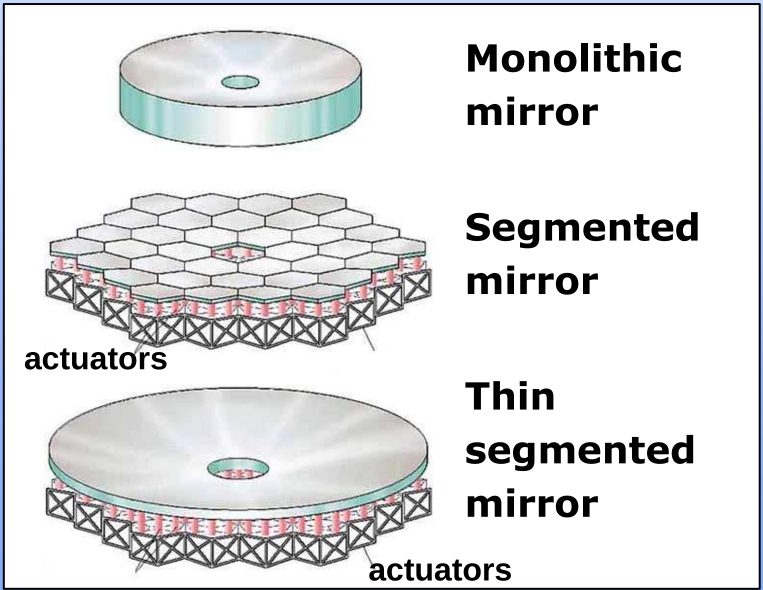

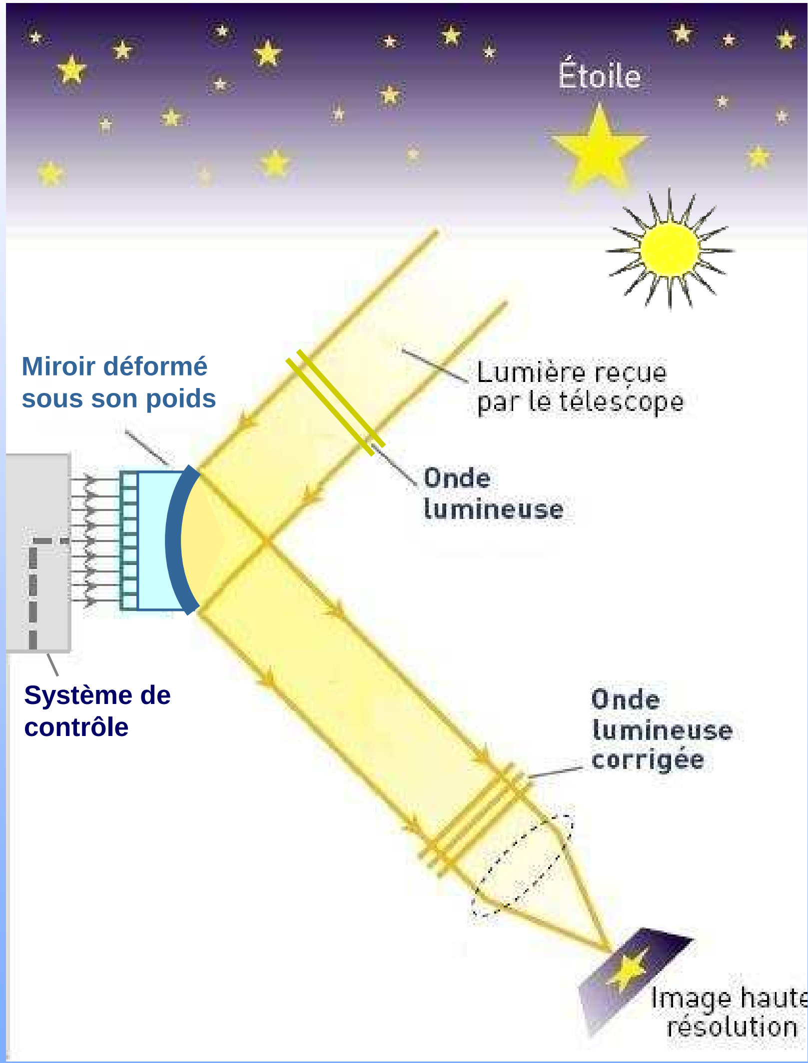

Active and Adaptive Optics

- Adaptive optics
  - **Close loop** operation
  - Refresh rate < 10 milliseconds
  - Correction applied to a special mirror (deformable mirror)
  - Requires additional optics
    - Dichroics
    - Wavefront sensors

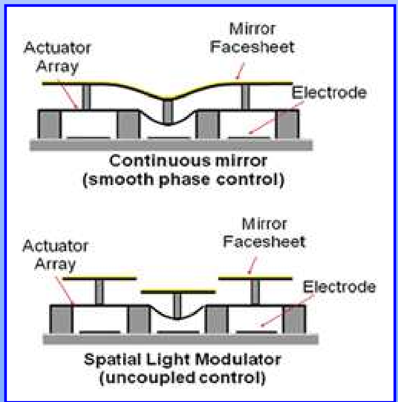

Continuous deformable mirror

Segmented deformable mirror

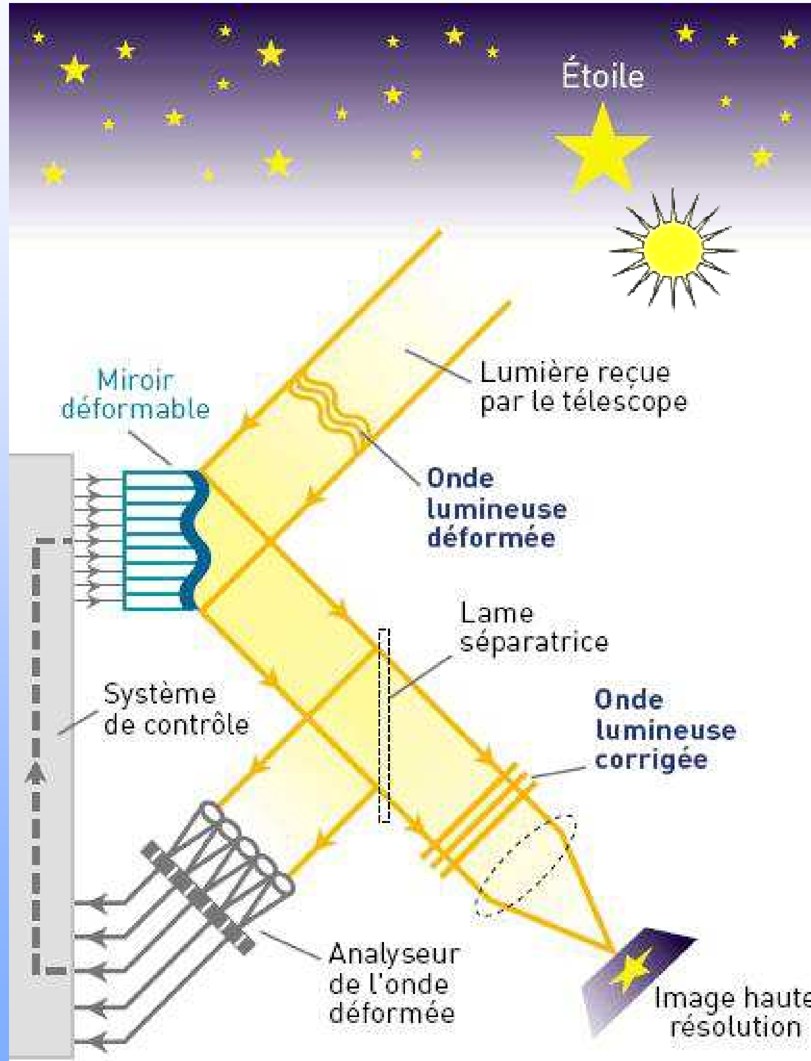

Atmospheric turbulence ("Seeing")

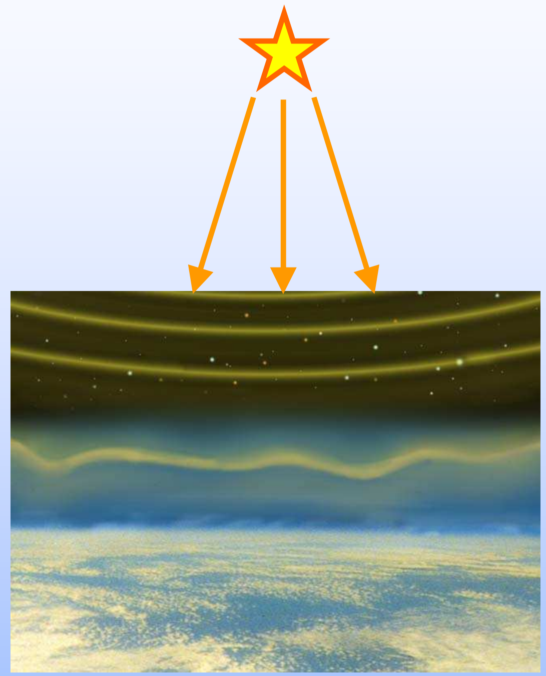

	Wavefront	Point spread function (PSF)
Moderate seeing		
Strong seeing		

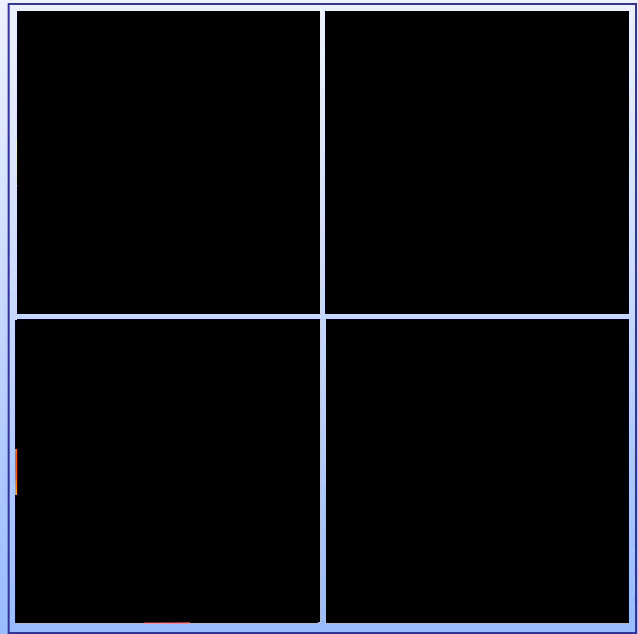

2 to 3 arcsec

All coming simulations for the second case (~ 6-7 λ PTV)

Elementary optical relations

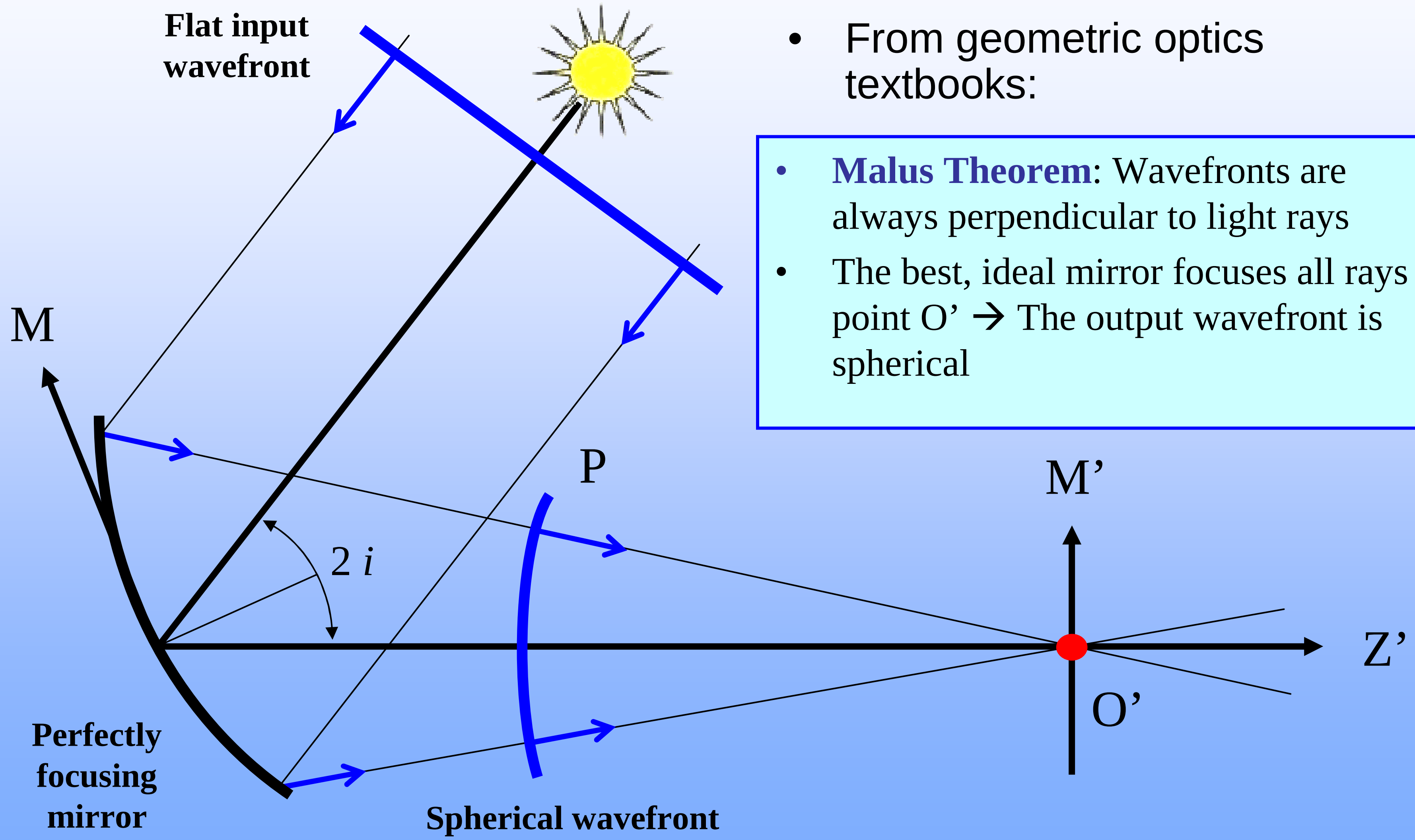

- From geometric optics textbooks:

- **Malus Theorem**: Wavefronts are always perpendicular to light rays
- The best, ideal mirror focuses all rays at point O’ → The output wavefront is spherical

Elementary optical relations

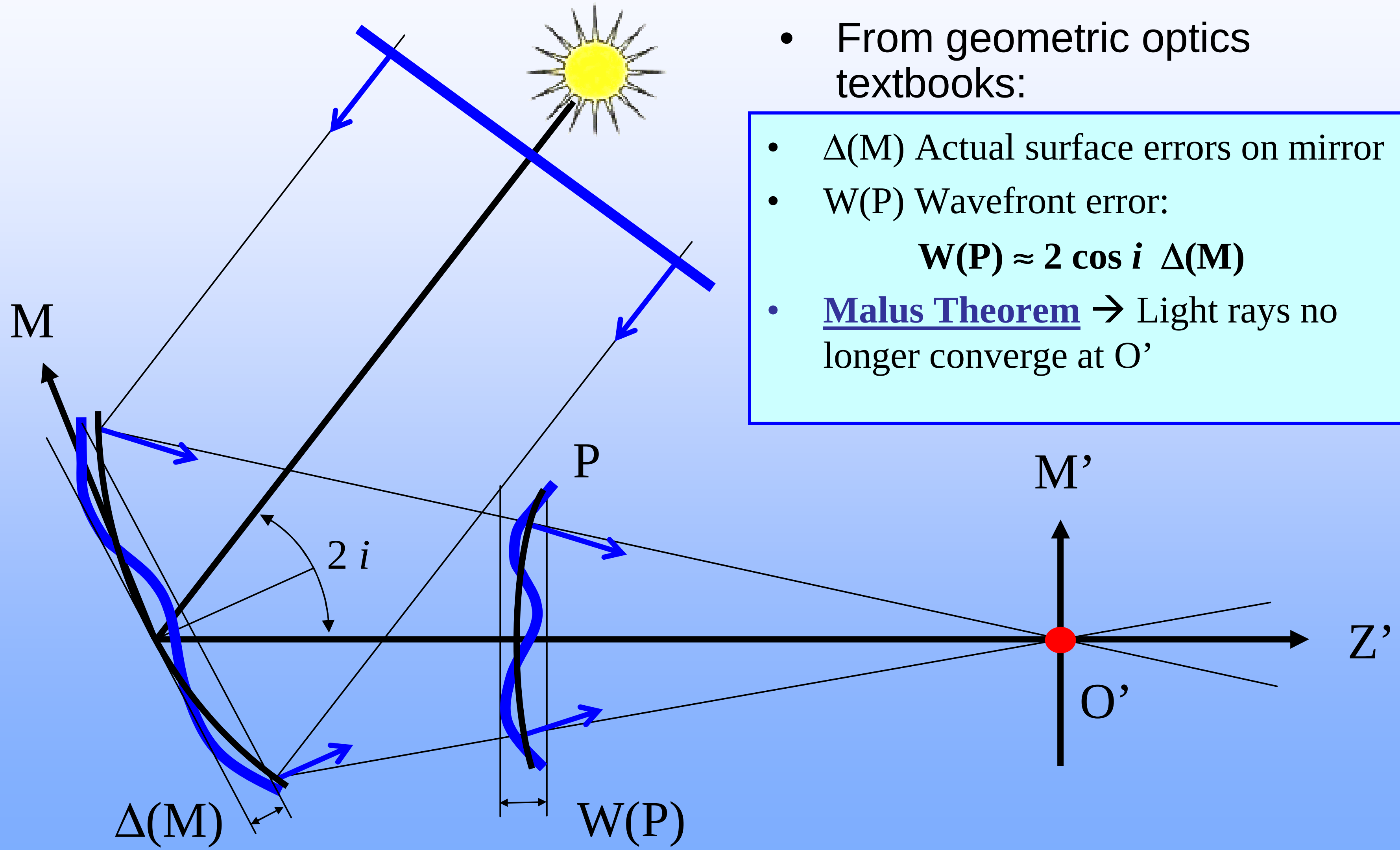

- From geometric optics textbooks:

- $\Delta(M)$ Actual surface errors on mirror
- $W(P)$ Wavefront error:

$$W(P) \approx 2 \cos i \;\; \Delta(M)$$

- **Malus Theorem** → Light rays no longer converge at O'

Elementary optical relations

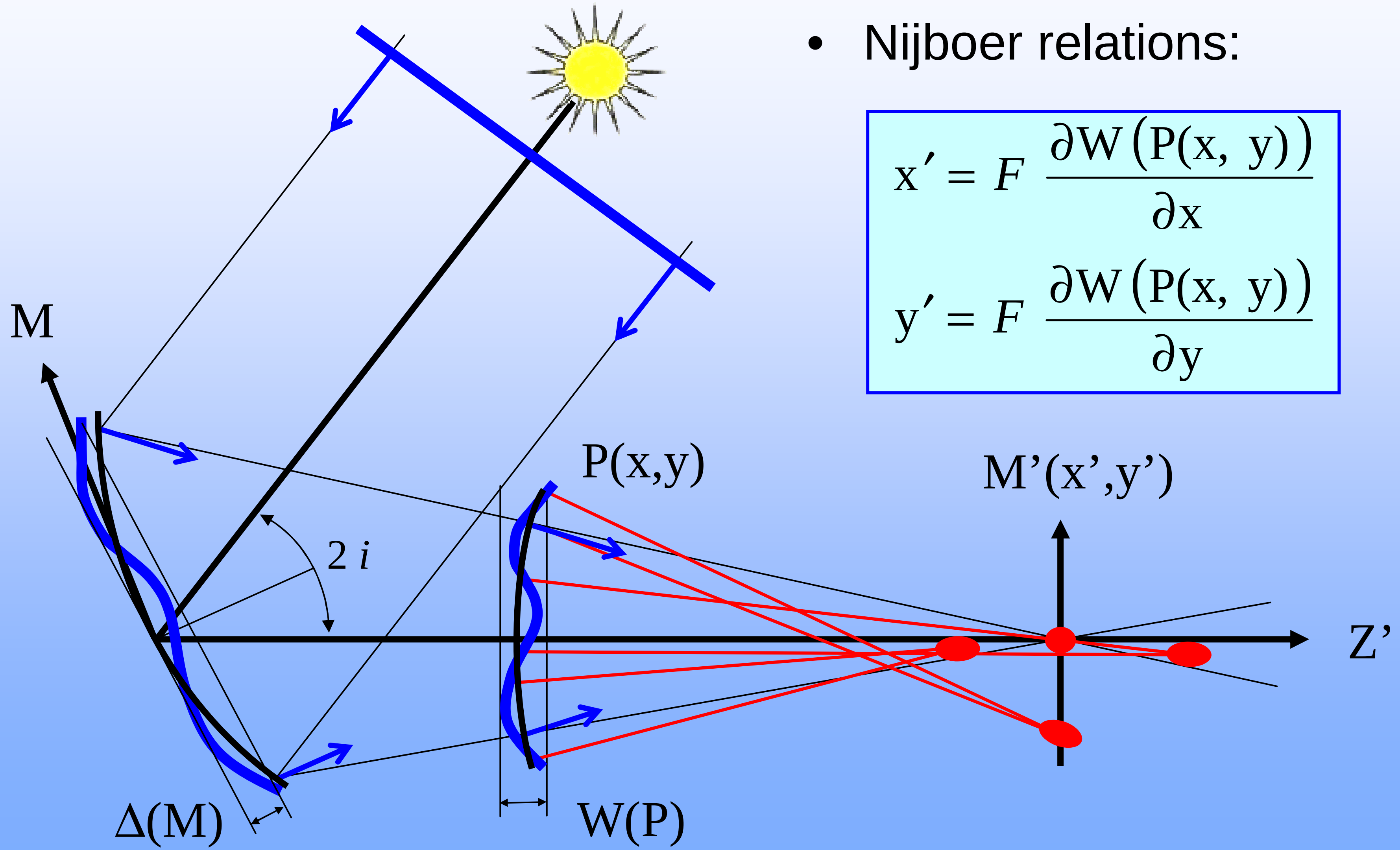

- Nijboer relations:

$$x' = F\,\frac{\partial W\left(P(x,\ y)\right)}{\partial x}$$

$$y' = F\,\frac{\partial W\left(P(x,\ y)\right)}{\partial y}$$

Elementary optical relations

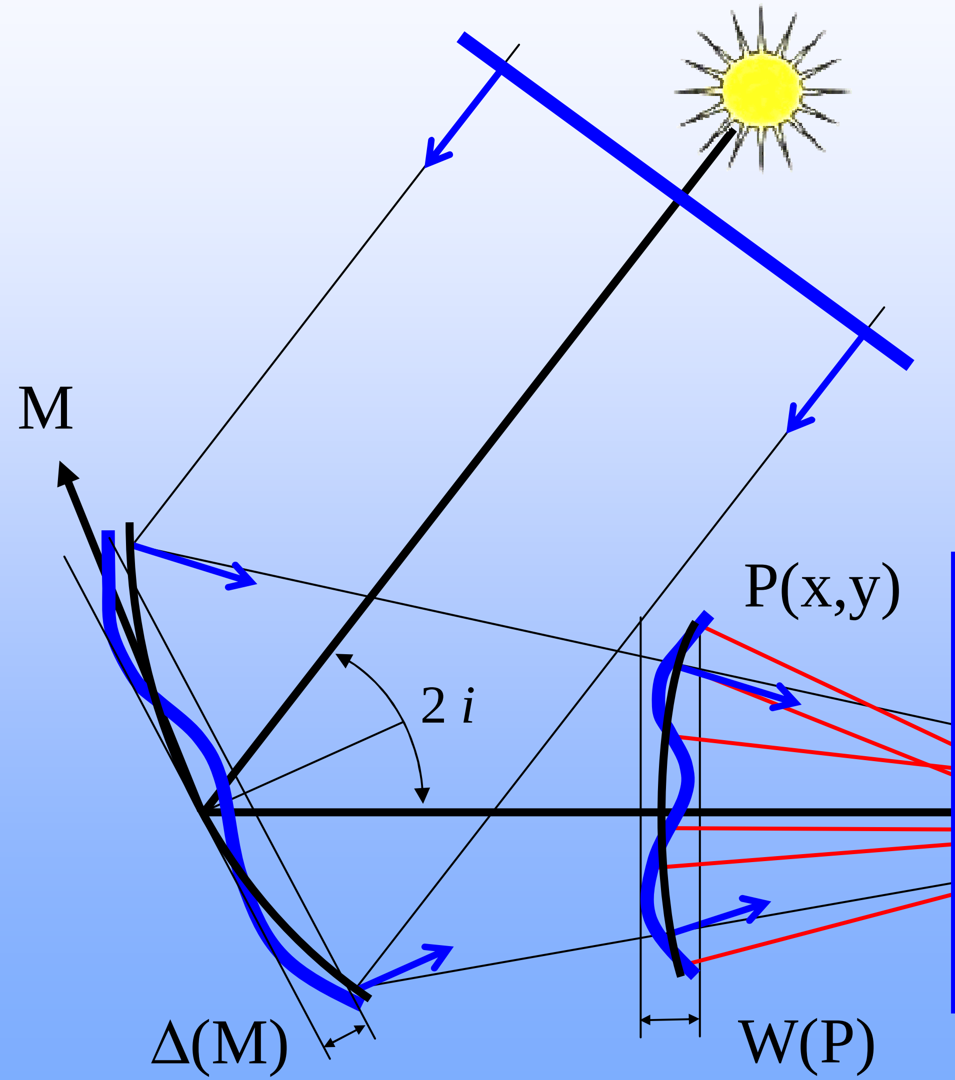

- Nijboer relations:

$$x' = F\,\frac{\partial W\left(P(x,\ y)\right)}{\partial x}$$

$$y' = F\,\frac{\partial W\left(P(x,\ y)\right)}{\partial y}$$

Generally speaking, a wavefront sensor does **not** sense wavefront, but its **partial derivatives**

Shack-Hartmann wavefront sensor

The most popular

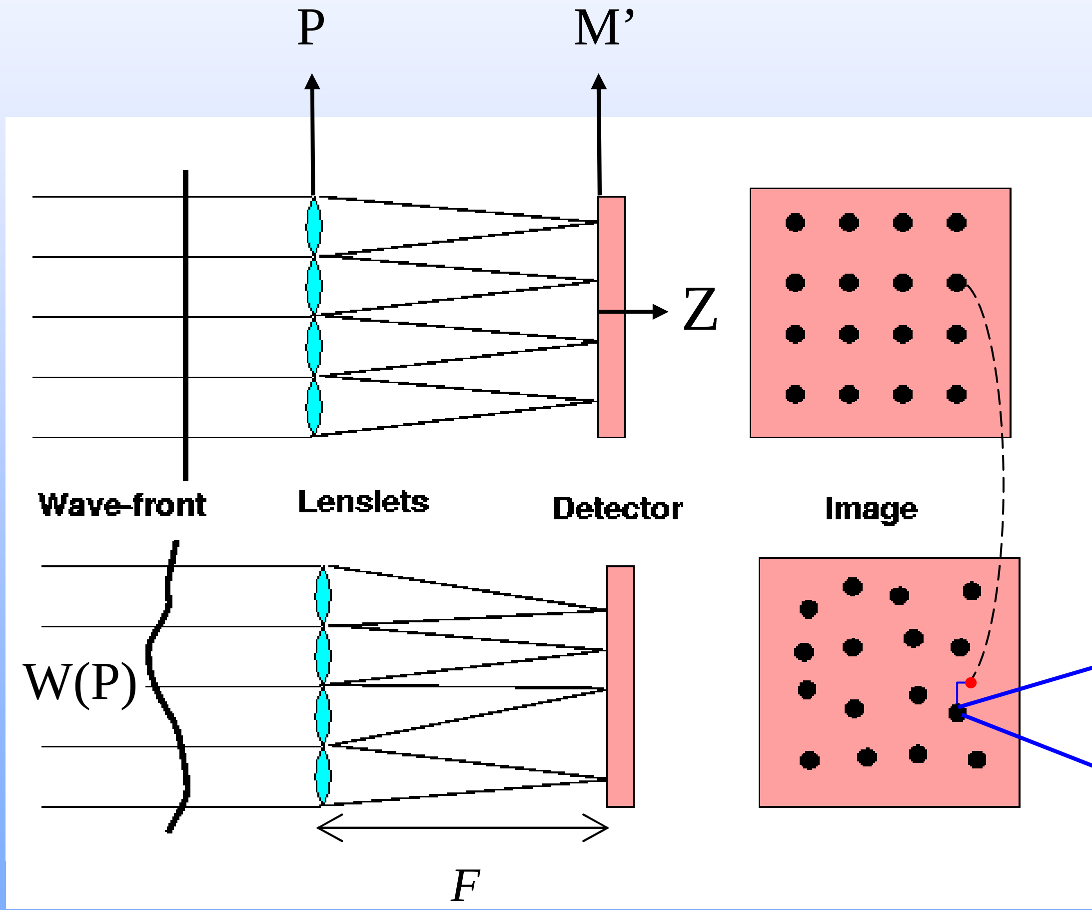

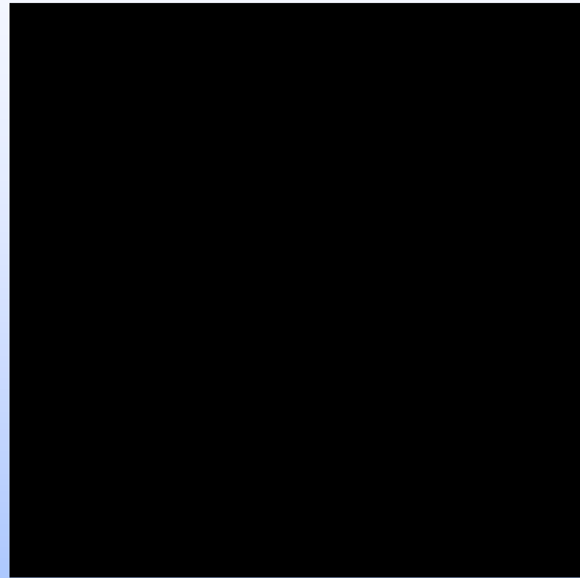

$$\delta x'_G(M') = F \frac{\partial W(P)}{\partial x}$$

$$\delta y'_G(M') = F \frac{\partial W(P)}{\partial y}$$

Curvature wavefront sensor

The most popular (in the 90’)

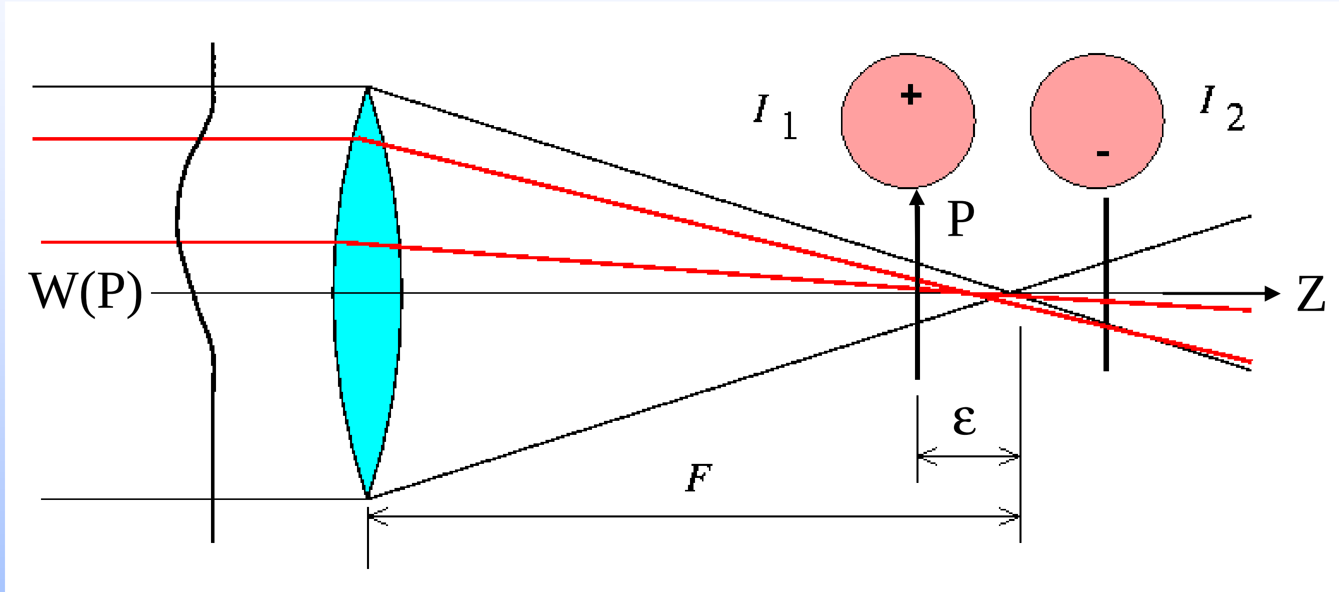

Intra-focus image

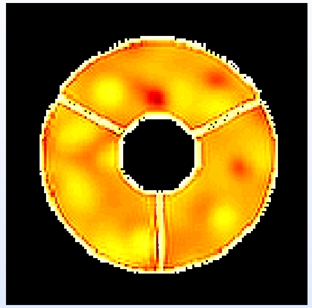

Extra-focus image

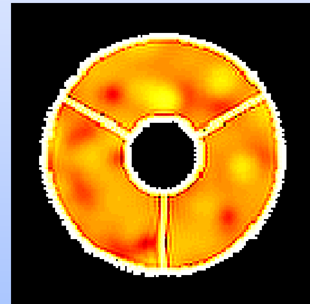

$$\frac{I_1(M) - I_2(P)}{I_1(M) + I_2(P)} = \frac{\lambda F\left(F-\varepsilon\right)}{2\pi\,\varepsilon}\left[\cancel{\delta_C(P)\frac{\partial W(P)}{\partial r}} - B_R(P)\left(\frac{\partial^2 W(P)}{\partial x^2} + \frac{\partial^2 W(P)}{\partial y^2}\right)\right]$$

- Makes use of the irradiance transport equation

Optical differentiation sensor (1/2)

Foucault test (XIXth Century)

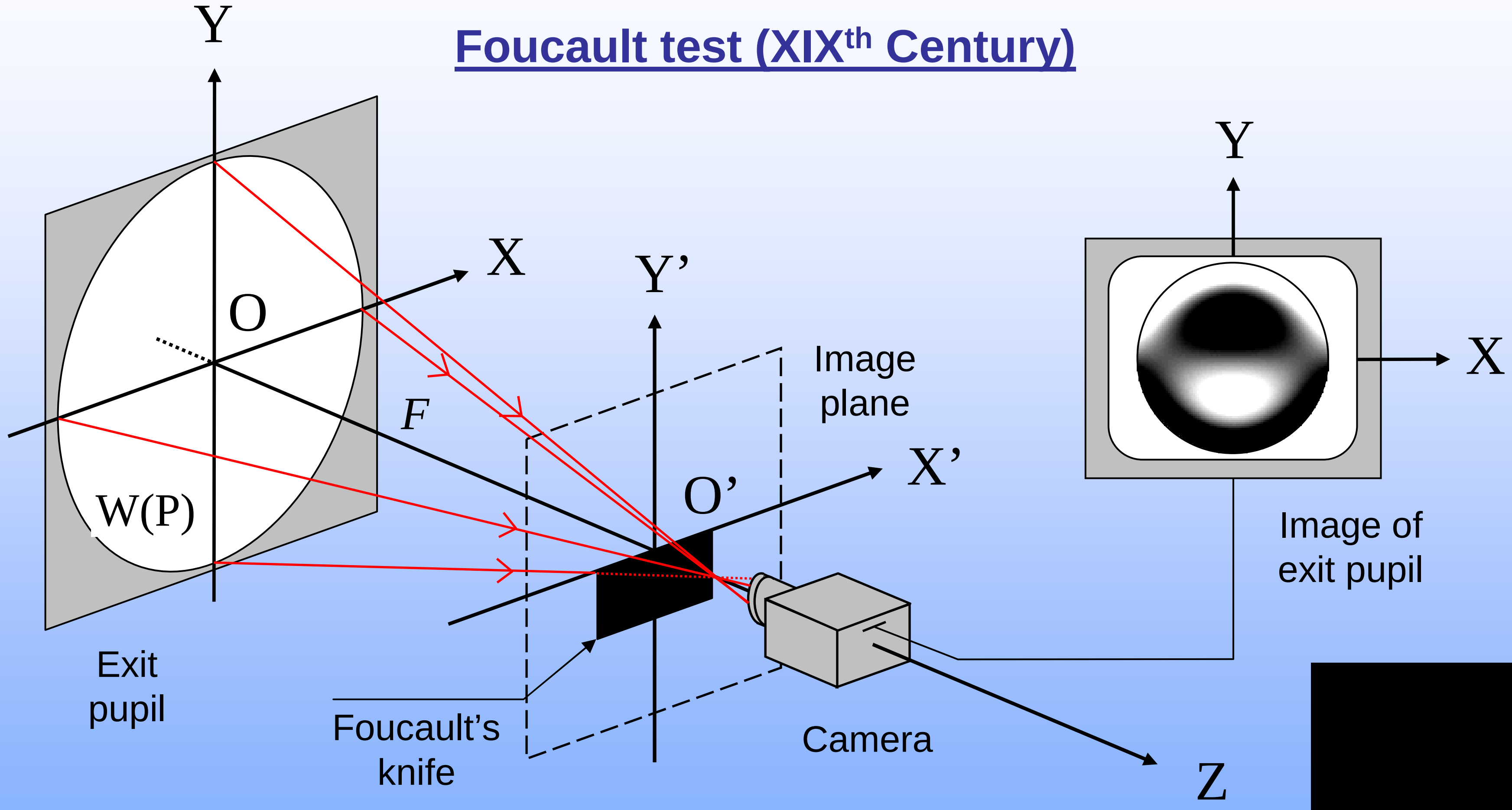

Optical differentiation sensor (2/2)

A quantitative Foucault test

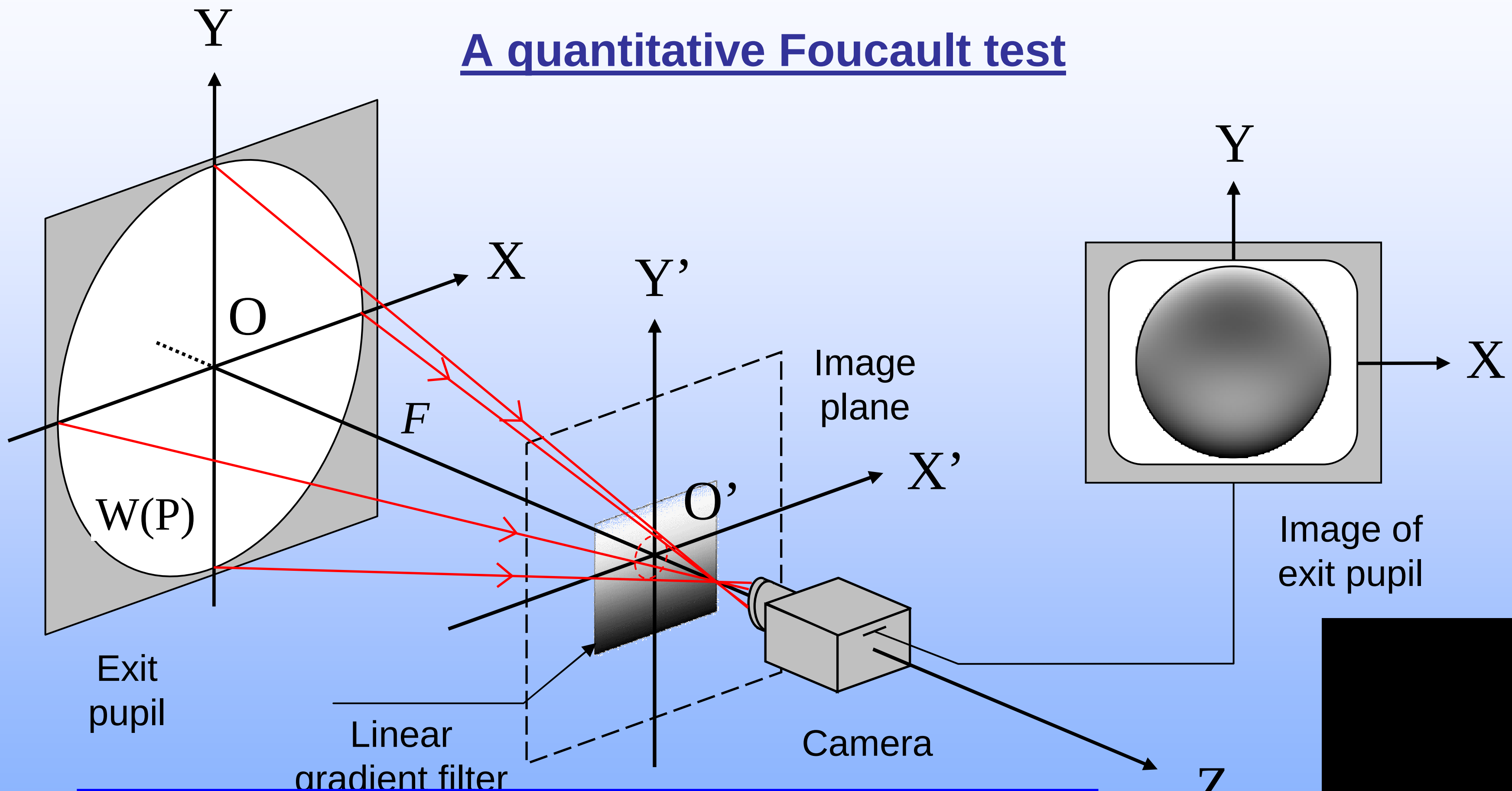

$$I_Y(P) = \frac{1}{4}\left| B_R(P)\left(1 + \frac{F}{y_1'}\frac{\partial W(P)}{\partial y}\right) - \cancel{i\,\frac{\lambda F}{2\pi y_1}\frac{\partial B_R(P)}{\partial y}}\right|^2$$

2005)

Pyramidal wavefront sensor

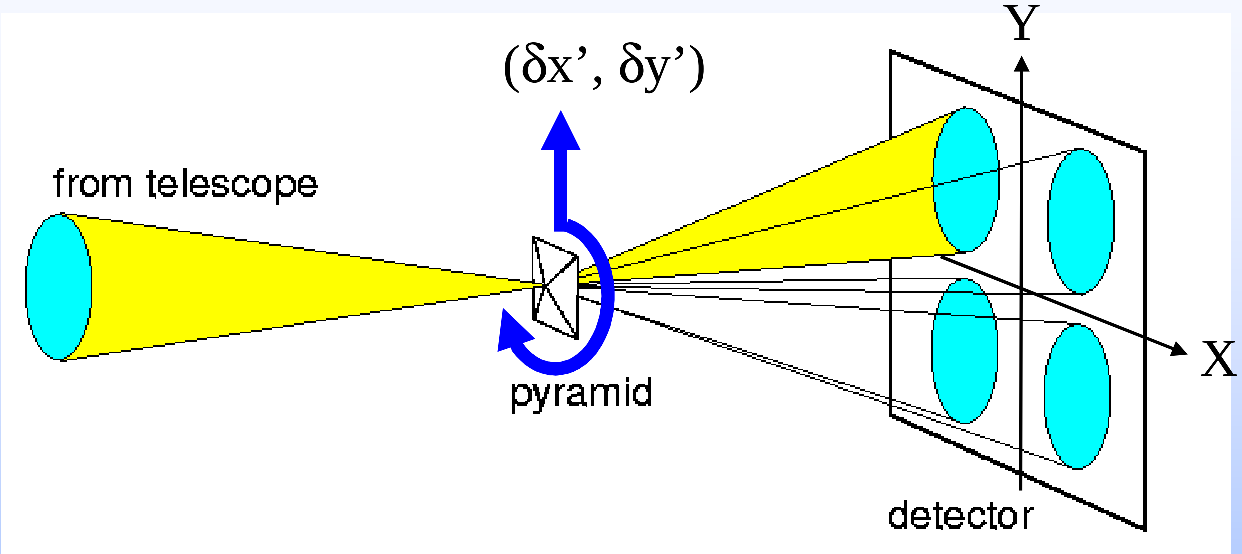

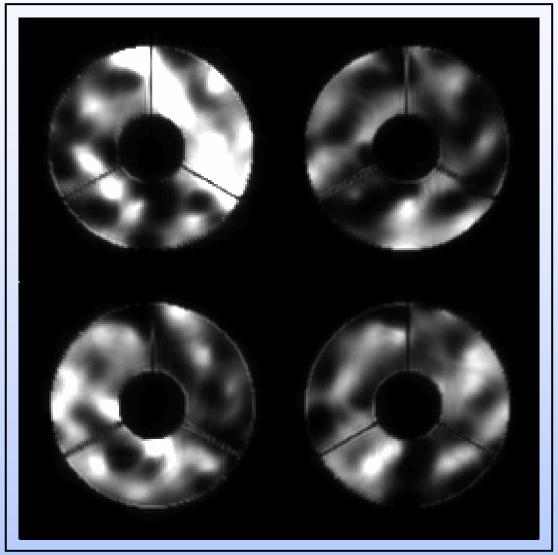

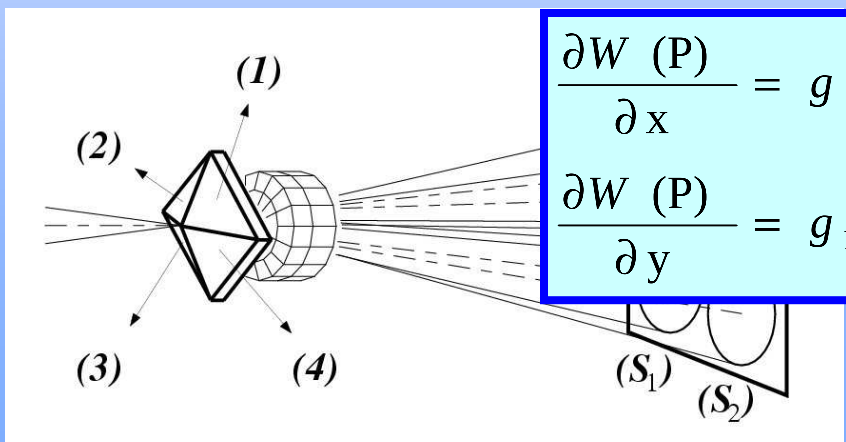

$$\frac{\partial W(P)}{\partial x} = g_X \frac{\delta x'}{F} \frac{\overline{S}_1(P) - \overline{S}_2(P) - \overline{S}_3(P) + \overline{S}_4(P)}{\overline{S}_1(P) + \overline{S}_2(P) + \overline{S}_3(P) + \overline{S}_4(P)}$$

$$\frac{\partial W(P)}{\partial y} = g_Y \frac{\delta y'}{F} \frac{\overline{S}_1(P) + \overline{S}_2(P) - \overline{S}_3(P) - \overline{S}_4(P)}{\overline{S}_1(P) + \overline{S}_2(P) + \overline{S}_3(P) + \overline{S}_4(P)}$$

Same relations as four-quadrants detector

Zernike wavefront sensor (Zelda)

The most recent

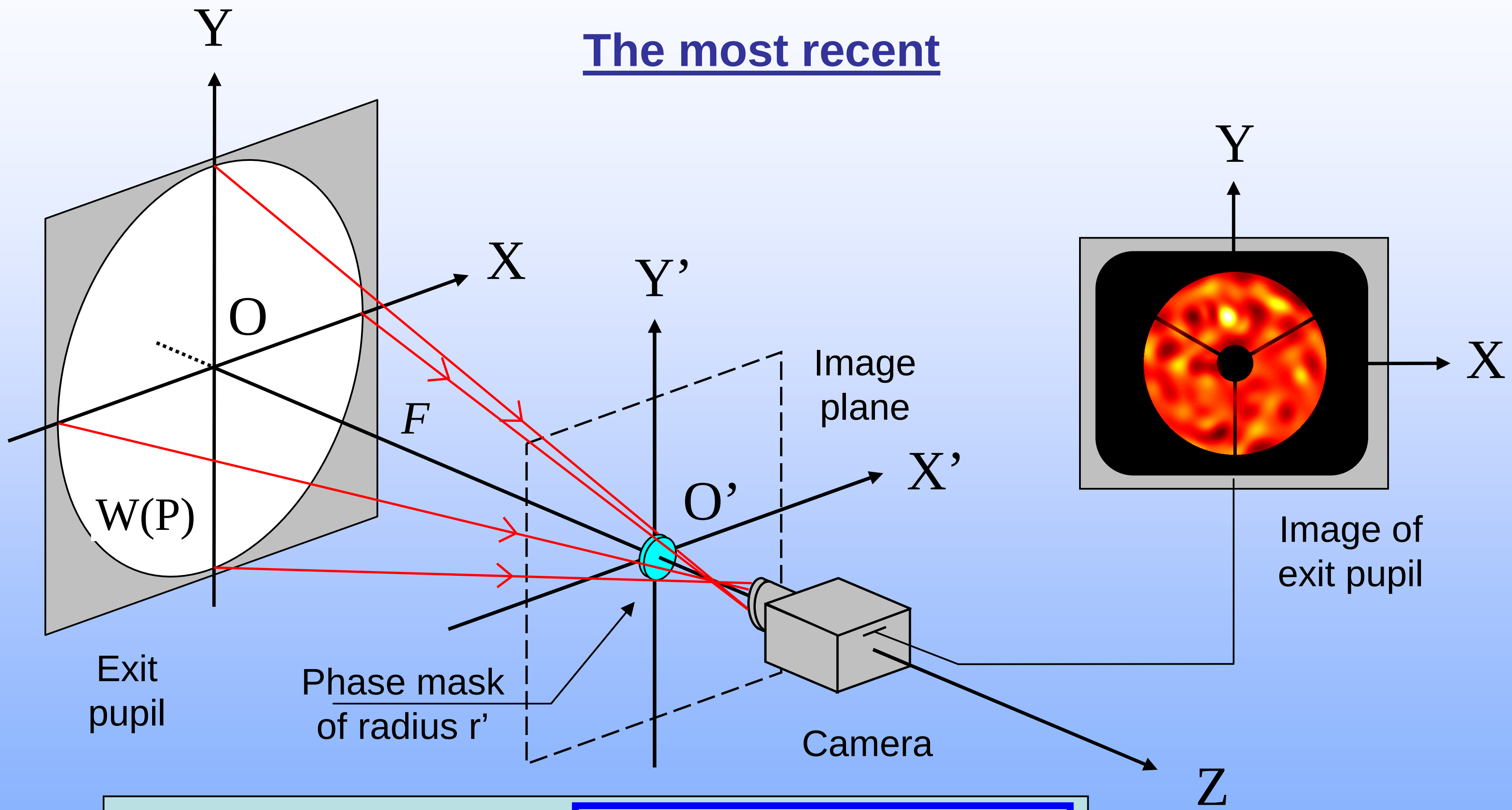

For a $\pi/2$ phase mask of radius $r' = 0.53\ \lambda\ N$

$$I(P) \approx B_R(P)\,\frac{\left(1+W(P)\right)^2}{2}$$

cs (2013)

Zernike wavefront sensor is very special

The only one that actually senses the wavefront

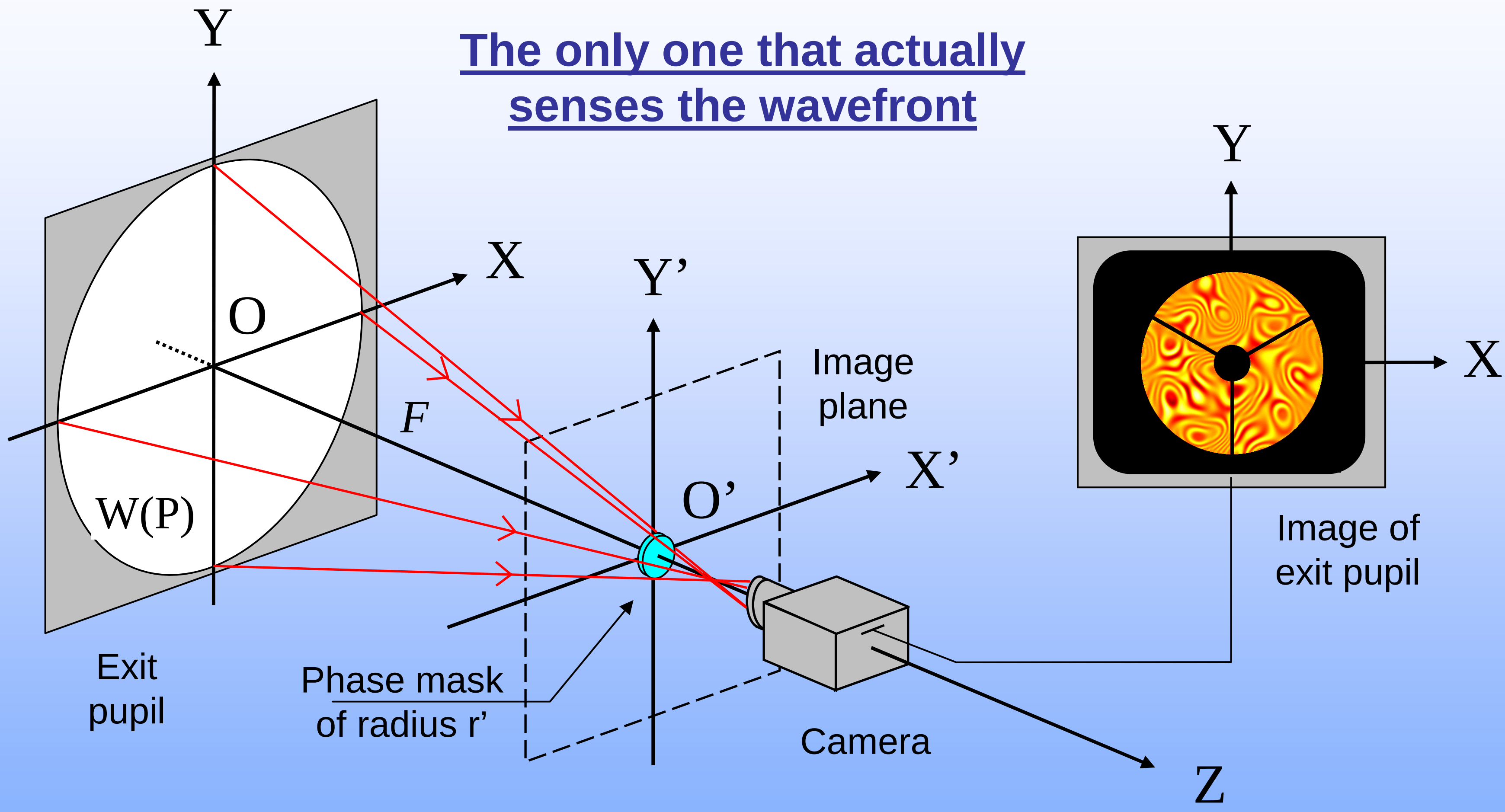

…But with **limited capture range**: [–λ/2, +λ/2] at the very best

A Ronchi-Reverse Hartmann wavefront sensor

F. Hénault, “Fresnel diffraction analysis of Ronchi and reverse Hartmann tests,” JOSA A vol. 35, p. 1717-1729 (2018)

Since 1920, the Ronchi test

One Hundred years old

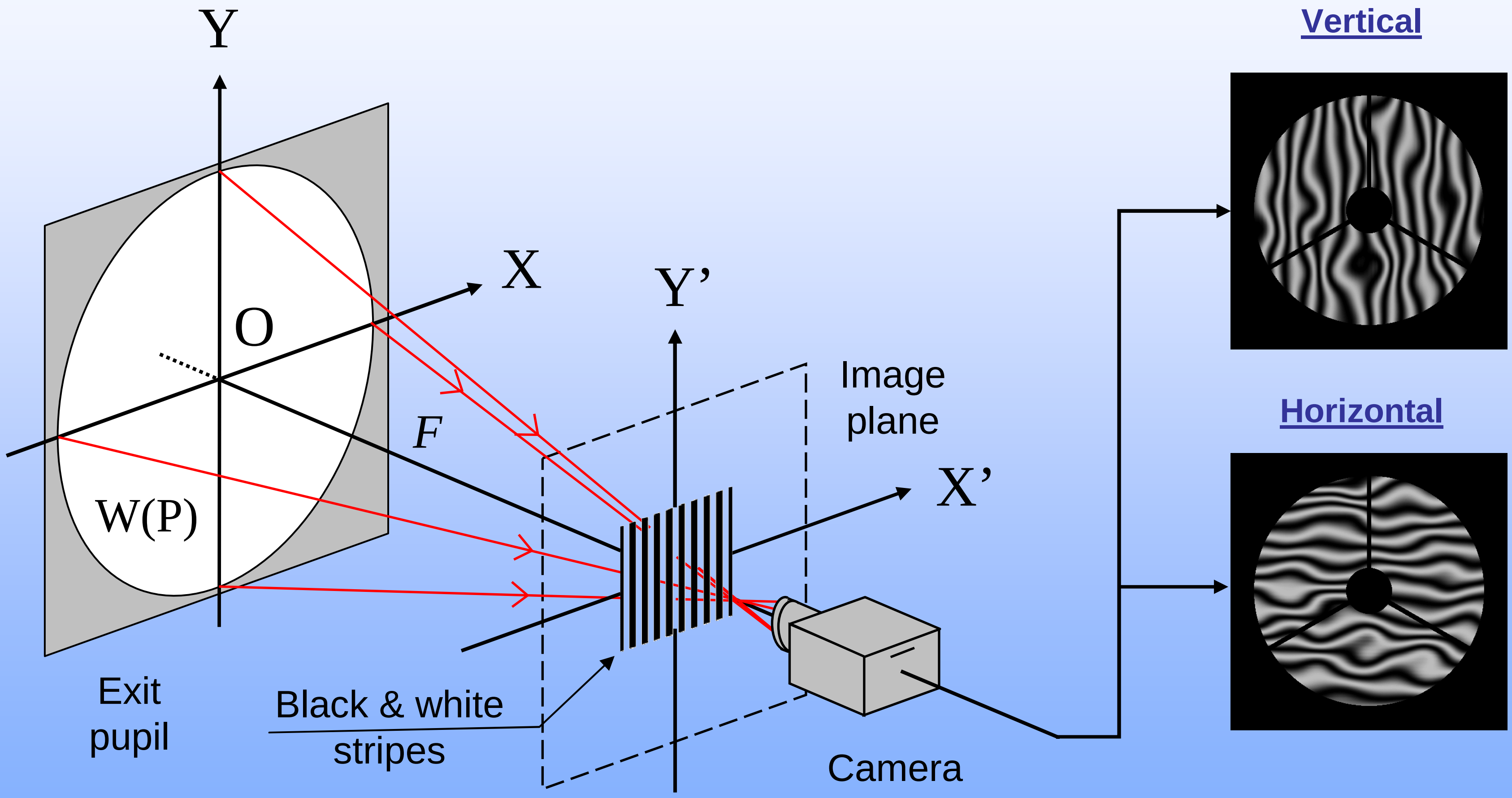

Since 1920, the Ronchi test

- Different interpretations: geometrical or physical optics
- Can only achieve quantitative results for some special parameters (e.g. defocus)
- In some cases, pupil replications due to diffraction grating effect

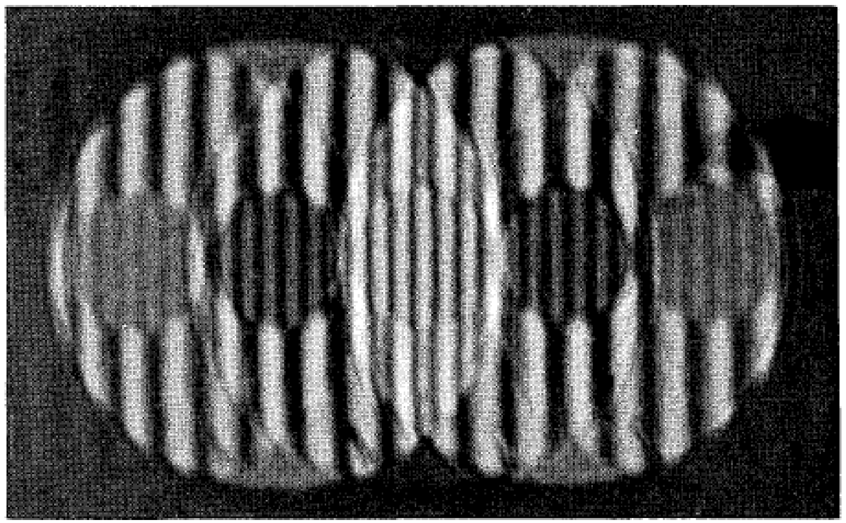

Fig. 8. The thinner fringes in the overlap region originating from higher-order interference.

Reverse Hartmann test

Hartmann or Shack- Hartmann:
- Mask at pupil, look at image plane

Reverse Hartmann:
- Mask near image plane, look at pupil

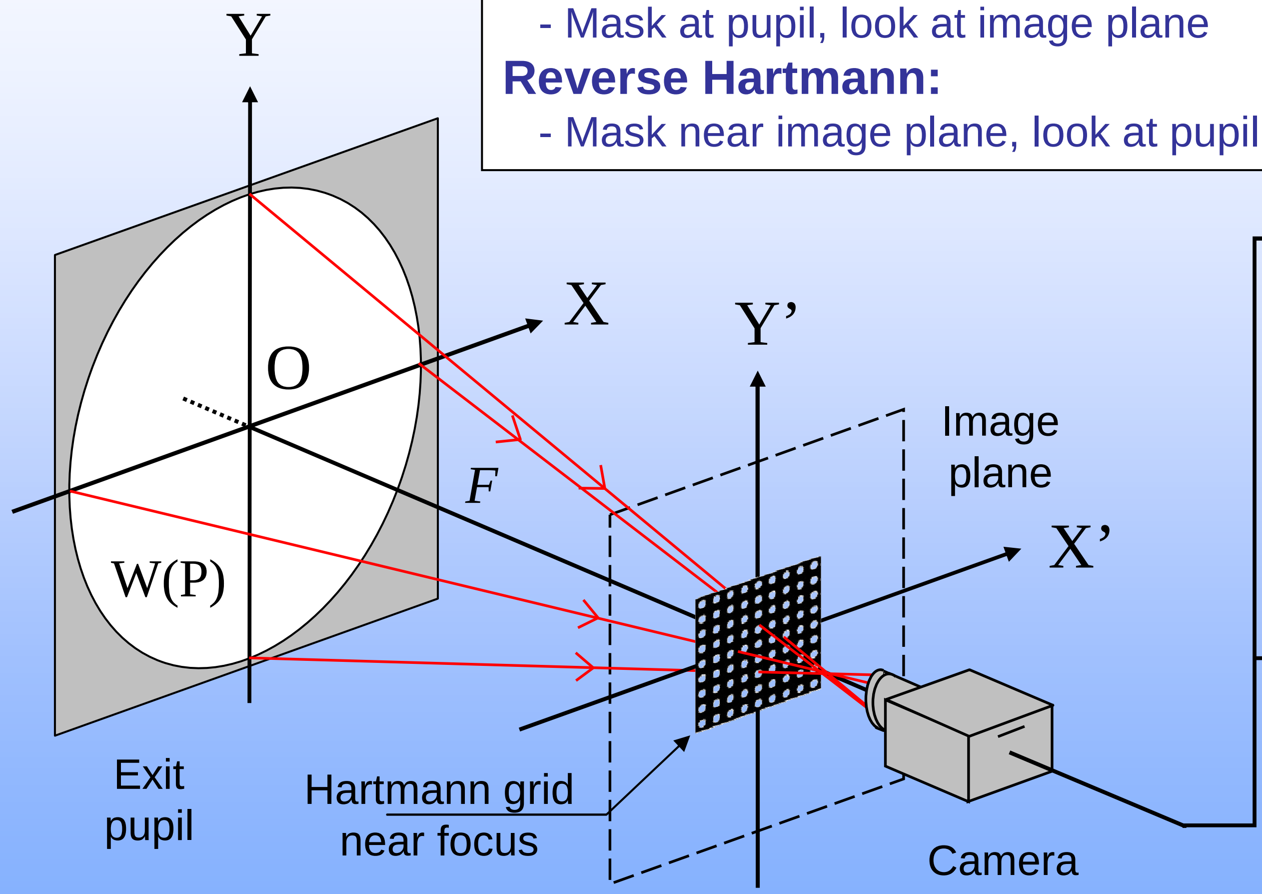

Pinholes array

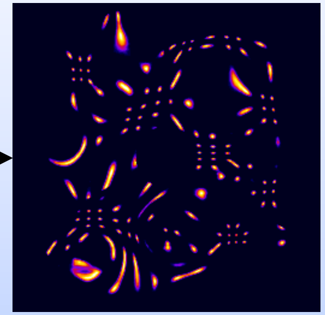

Grid

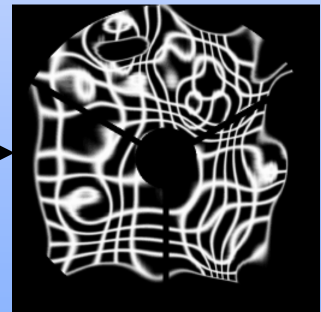

Analytical and numerical model

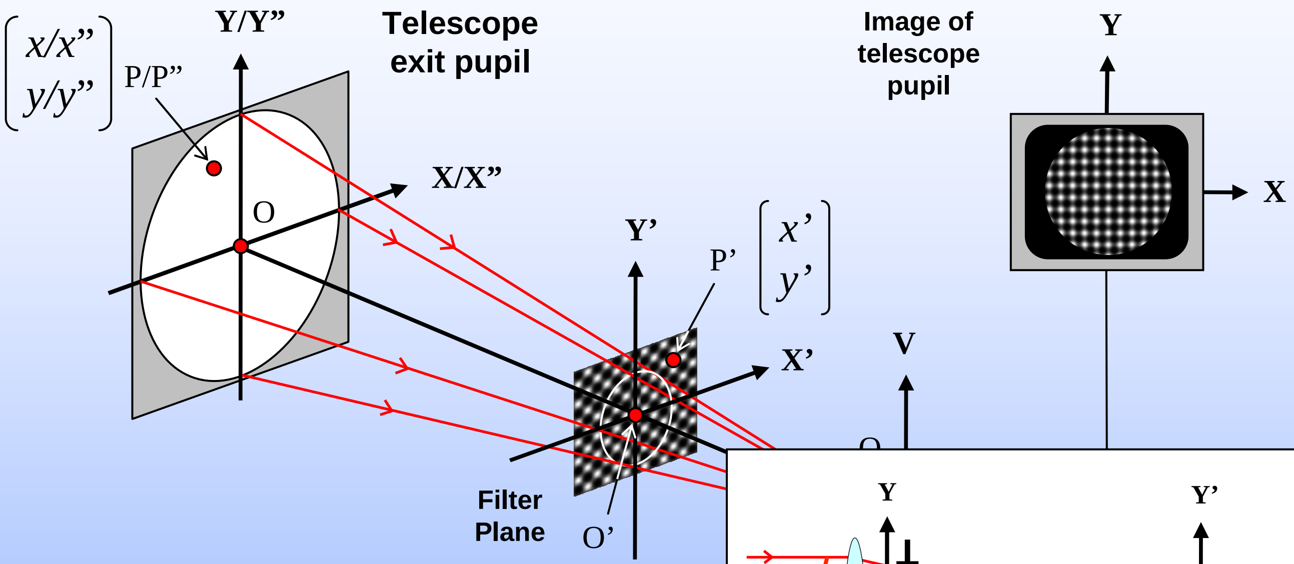

The model can be simplified by retro-propagating complex amplitude from the filter to the pupil planes

- In the most general case the spatial filter is not located at pupil or image planes
- Use of a Fresnel diffraction model is mandatory

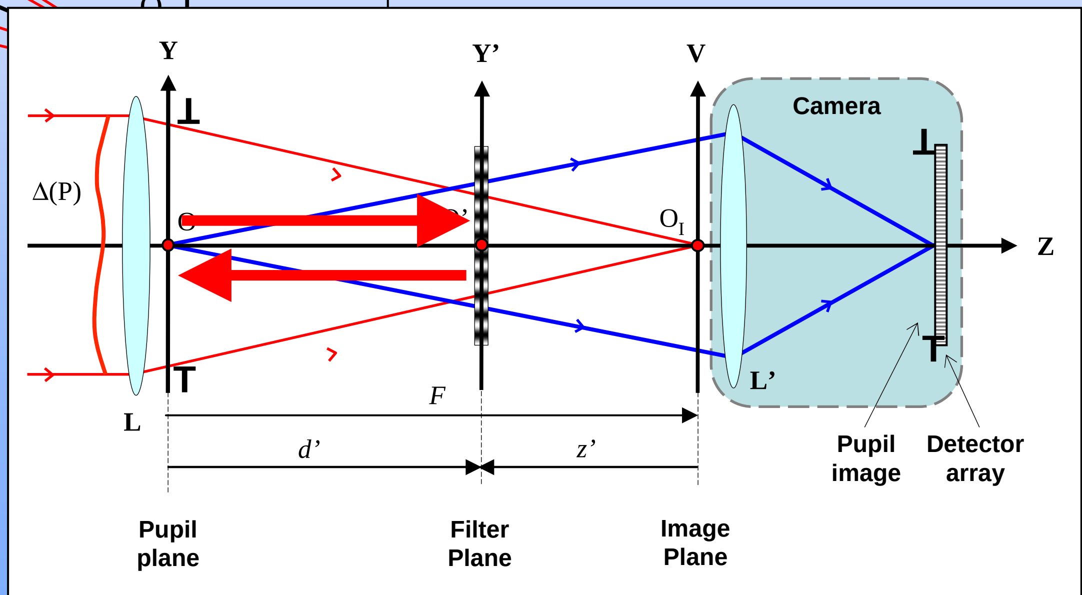

Different types of spatial filter

Binary Ronchi grating | **Sinusoidal Ronchi grating** | **Square Ronchi grating** | **Hartmann grid (pinholes)**

Filter transmission

$\mathrm{T}(x', y')$

Power spectrum

$\left|FT\left[\mathrm{T}(x', y')\right]\right|^2$

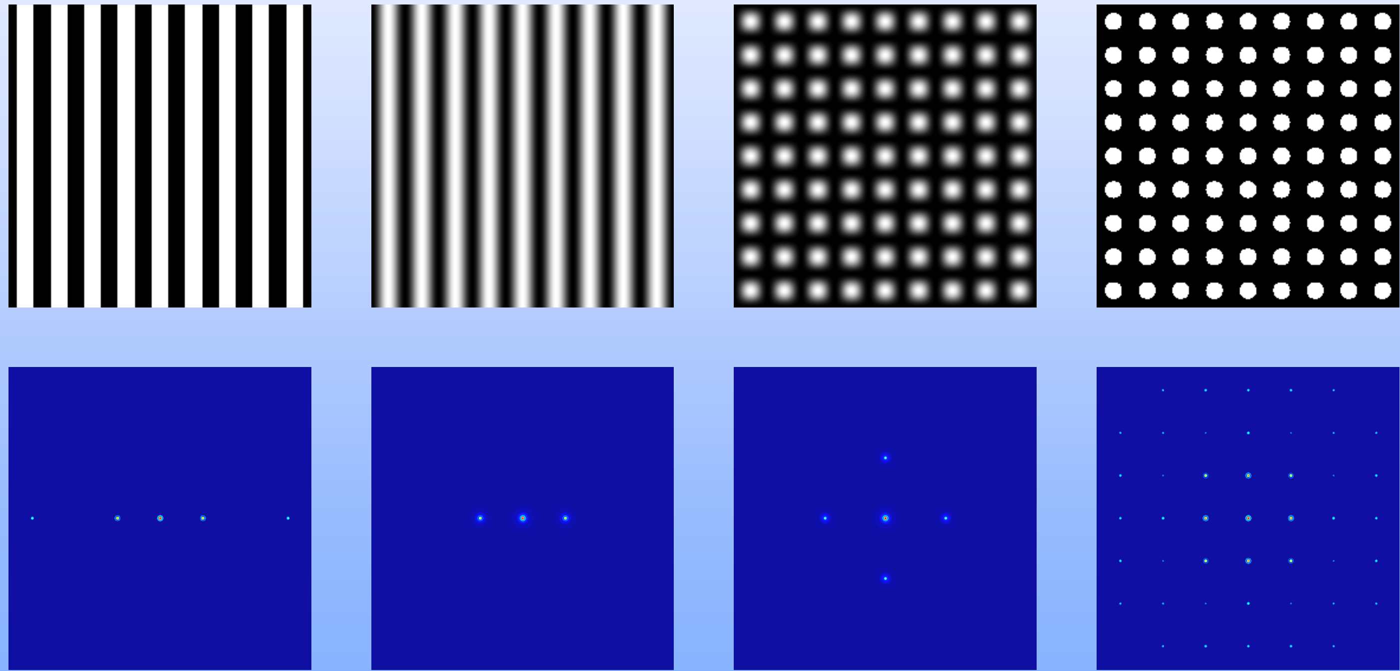

Numerical simulation of pupil images

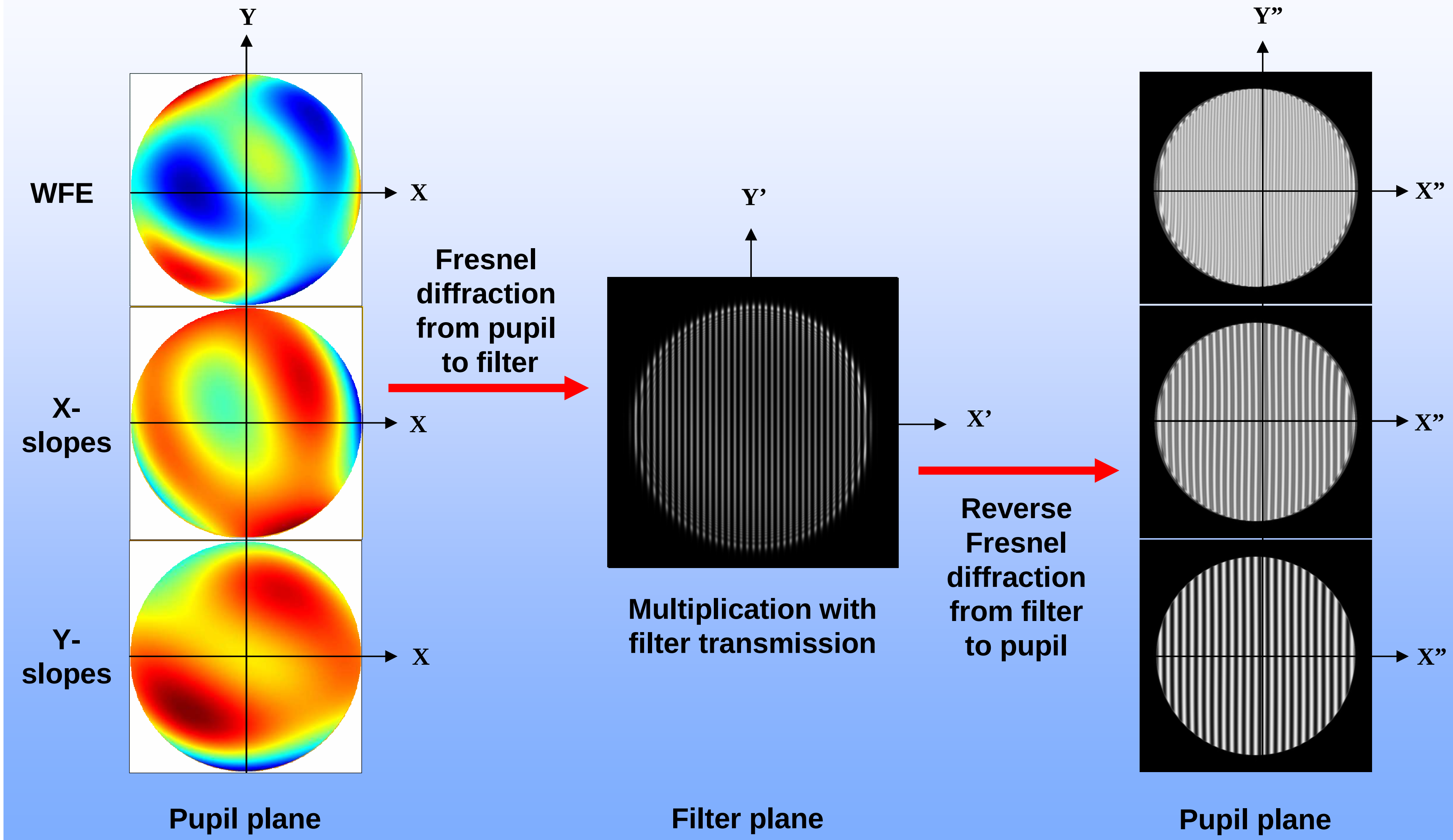

Wavefront slopes reconstruction

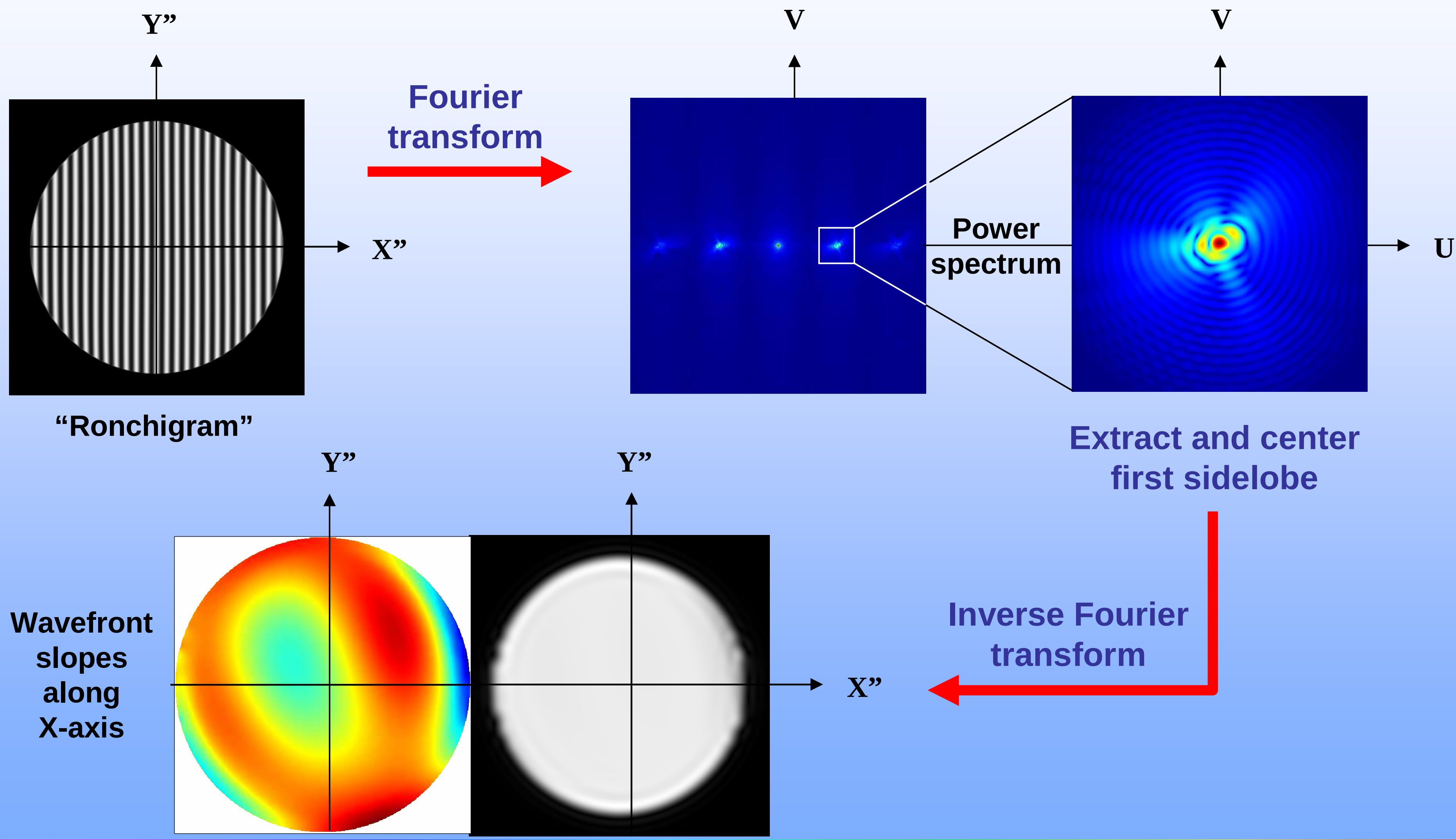

Optimizing the system

- Need to find best compromise between various criteria
  - Relative pupil shift ➦ $\rho = \lambda N \left(1 + z'/F\right)/p$
  - Gain ➤ $g = 2\pi \left(F + z'\right)/p$
  - Lines number over pupil ➤ $n_M = |z'| f / N$
  - Contrast ➤ (see next slide)

λ	Wavelength
N	Aperture number
F	Focal length
z'	Distance from focus to pupil
p	Filter spatial period

- Can be done by using minimization algorithms (Newton, Powell, etc.)

Merit function

$$MF = \sum_{i=1}^{4} w_i \left(C_i - T_i\right)^2$$

i	Goal	Criteria C_i	Targets T_i
1	Minimize relative pupil shear to improve resolution	$C_1 = \rho$	$T_1 = 0$
2	Maximize gain (SNR)	$C_2 = 1/g$	$T_2 = 0$
3	Ensure minimal fringe number to avoid aliasing	$C_3 = \mathrm{Min}(n_M, T_3)$	$T_3 = 50$
4	Maximize contrast (SNR)	$C_4 = \mathrm{Min}(C(\lambda), T_4)$	$T_4 = 0.8$

Optimizing the contrast

- Monochromatic and polychromatic contrast can be plotted as functions of variables *z*' and *f* = 1/*p*
- It shows many possibilities for achieving high contrast

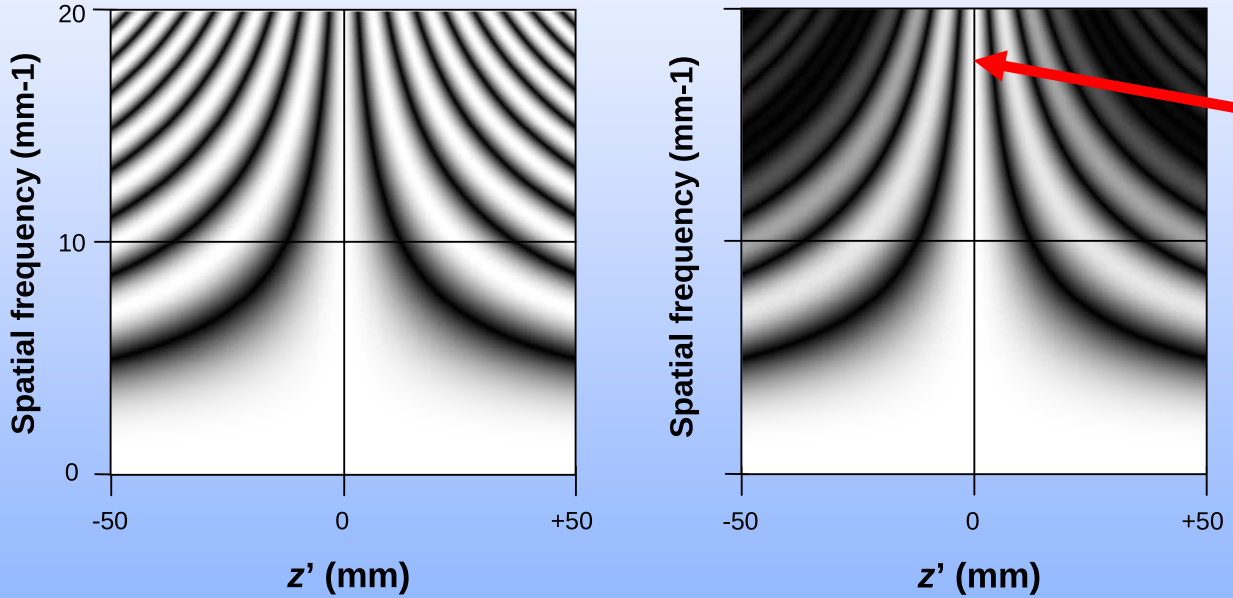

Rule of thumb
Associate small *z*' distances with high filter spatial frequencies

$$C(\lambda) = \cos\left[\pi\lambda \frac{z'F\left(1+z'/F\right)}{p^2}\right]$$

$$C_{\delta\lambda}(\lambda_0) = \operatorname{sinc}\left[\pi \frac{\delta\lambda}{2} \frac{z'F\left(1+z'/F\right)}{p^2}\right] C(\lambda_0)$$

Monochromatic **Polychromatic δλ/λ = 10%**

Numerical simulations

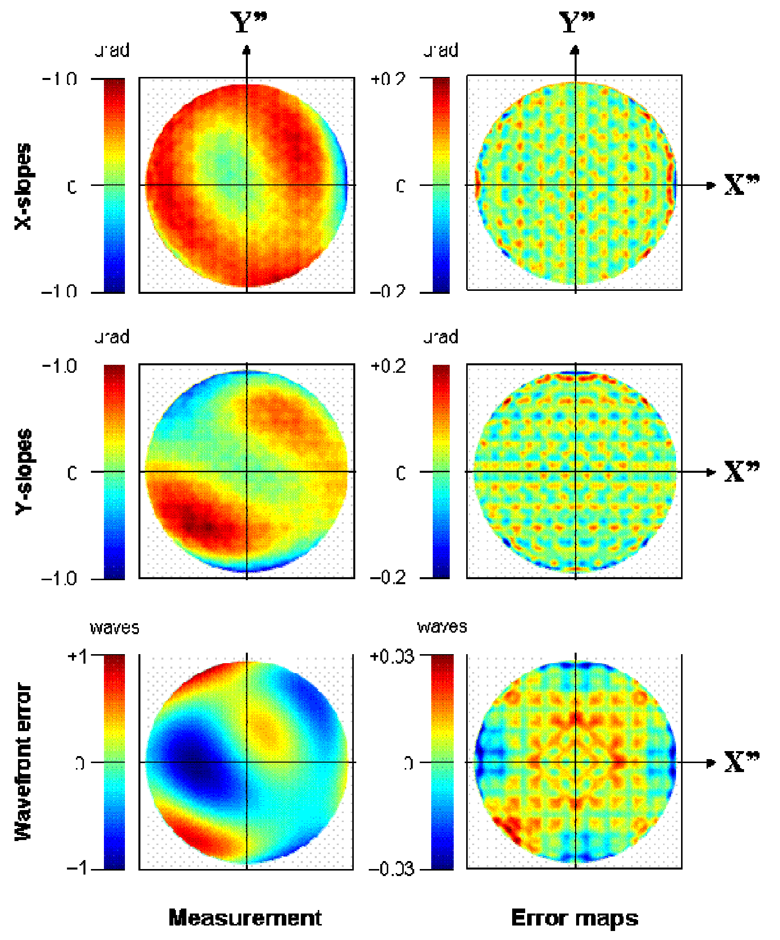

Mirror test with Hartmann grid

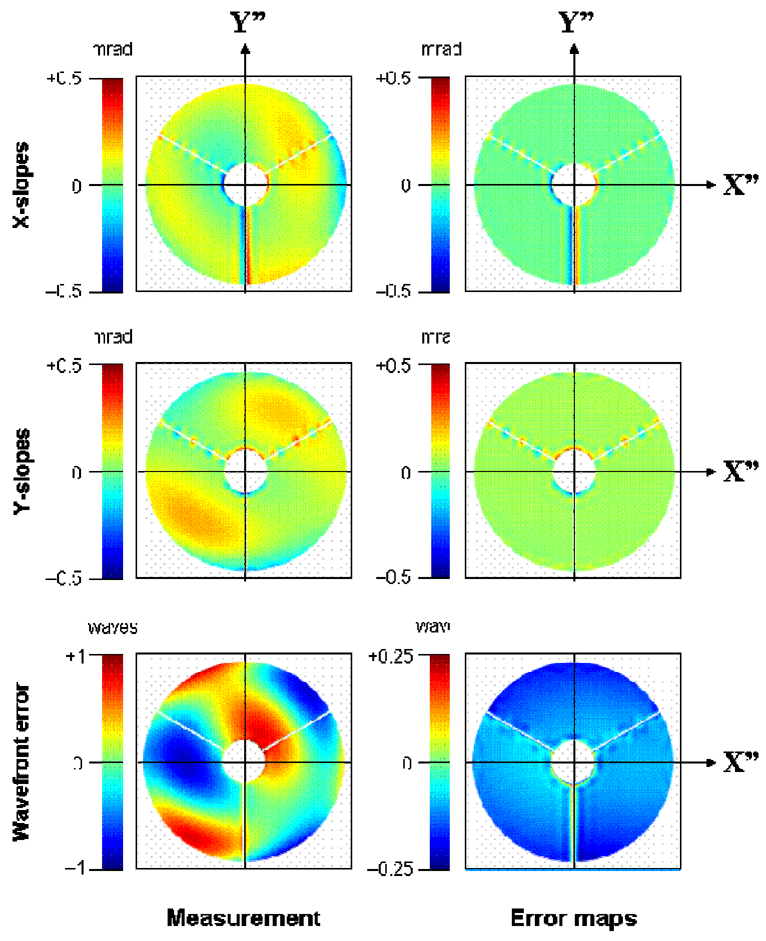

Wavefront sensor with square Ronchi grid

Numerical results

	Single mirror / Test method								
	Square Ronchi test				**Reverse Hartmann test**				
Error type	Original	Measured	Difference	Relative error (%)	Original	Measured	Difference	Relative error (%)	
X-slopes (µrad)	1.790 0.278	2.040 0.282	0.535 0.023	30 8	1.790 0.278	2.111 0.281	0.449 0.043	25 15	PTV RMS
Y-slopes (µrad)	1.966 0.328	2.170 0.330	0.508 0.023	26 7	1.966 0.328	2.200 0.333	0.411 0.042	21 13	PTV RMS
WFE (waves)	1.761 0.340	1.770 0.342	0.049 0.004	3 1	1.761 0.340	1.763 0.341	0.073 0.010	4 3	PTV RMS

Error ty	
X-slopes (n	PTV RMS
Y-slopes (n	PTV RMS
WFE (wav	PTV RMS

Absolute measurement accuracy ranges from $\lambda/30$ to $< \lambda/100$ RMS in different cases

- Spatial filter: Square Ronchi ➤ or Hartmann ➦
- Numerical aperture: High ➤ or low ➦
- Spectral range: Visible ➤ or near IR ➦

For Harmoni LGSS people only

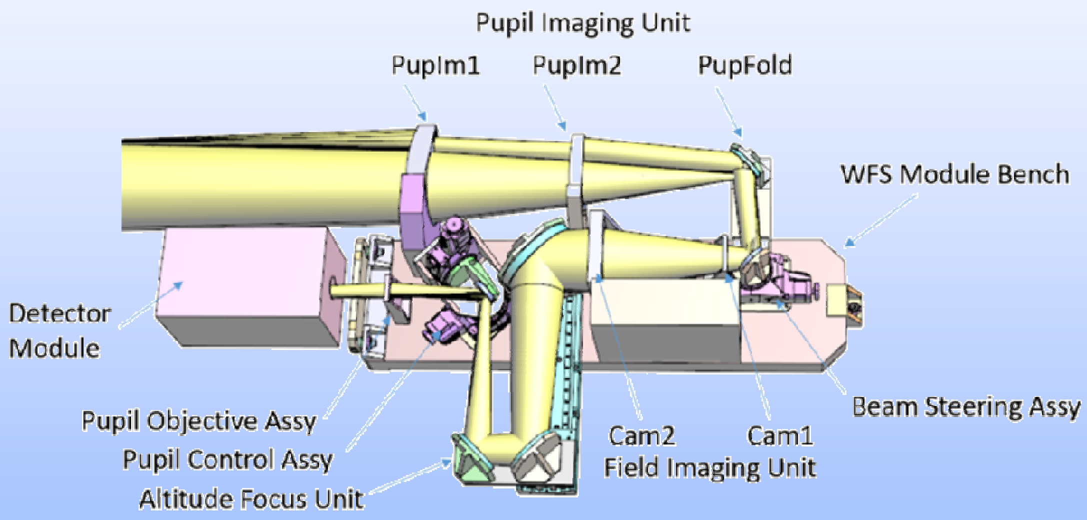

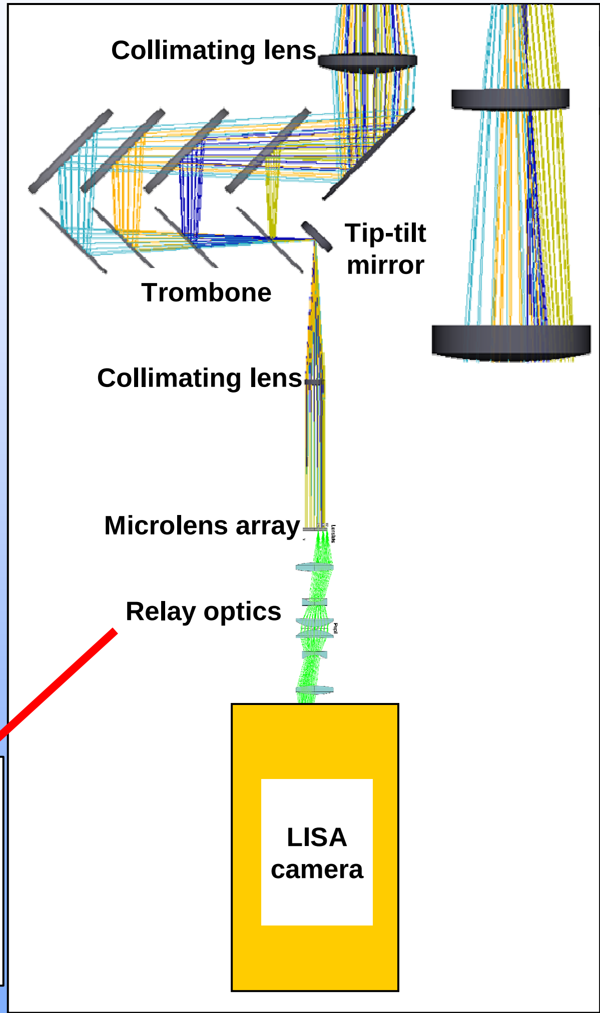

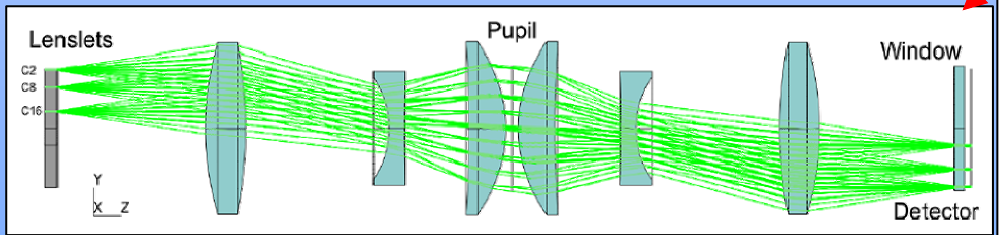

For Harmoni LGSS people only

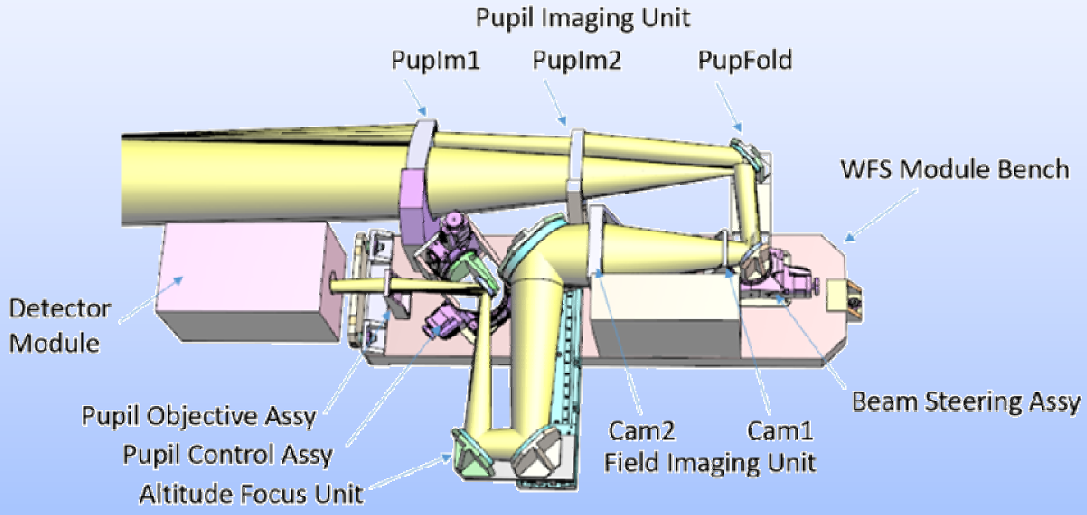

Laser Guide Star Subsystem (LGSS) for Harmoni ELT instrument

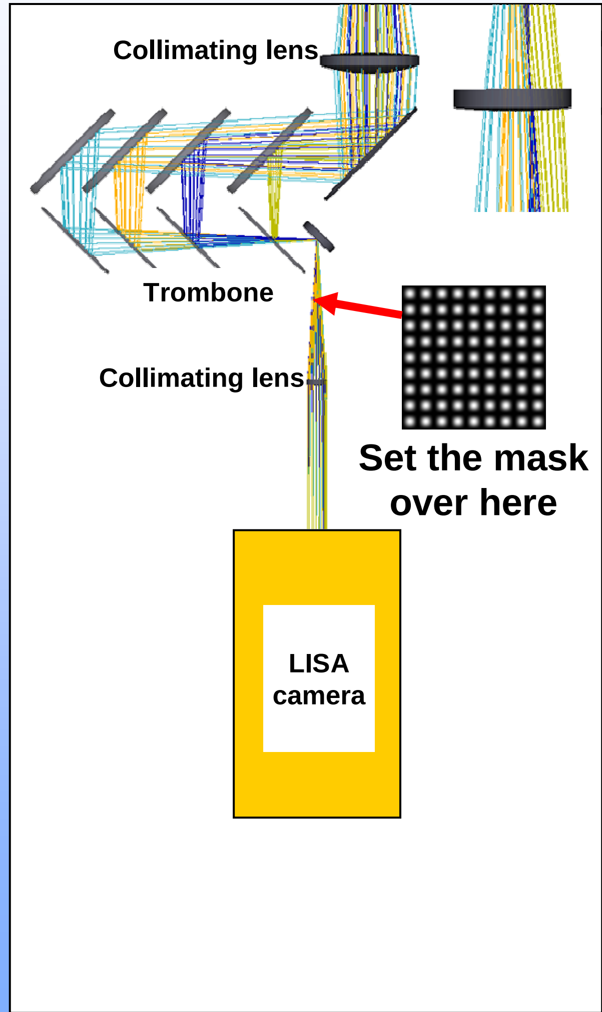

Reverse Hartmann wavefront sensor

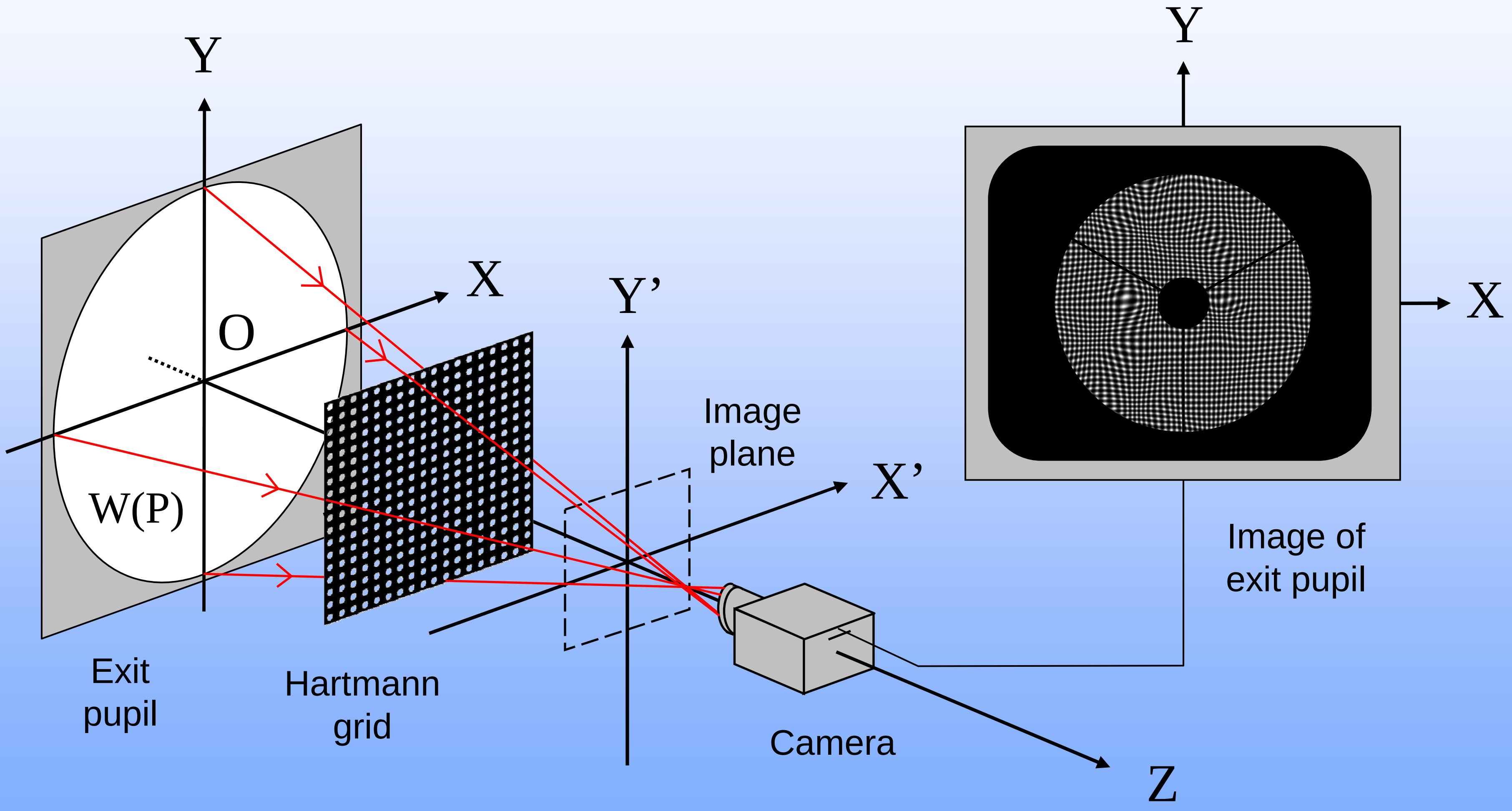

Operating from behind a coronagraph mask

F. Hénault, A. Carlotti, C. Vérinaud, “Phase-shifting coronagraph,” Proceedings of the SPIE vol. 10400 (2017)

Look at pupil trough phase masks

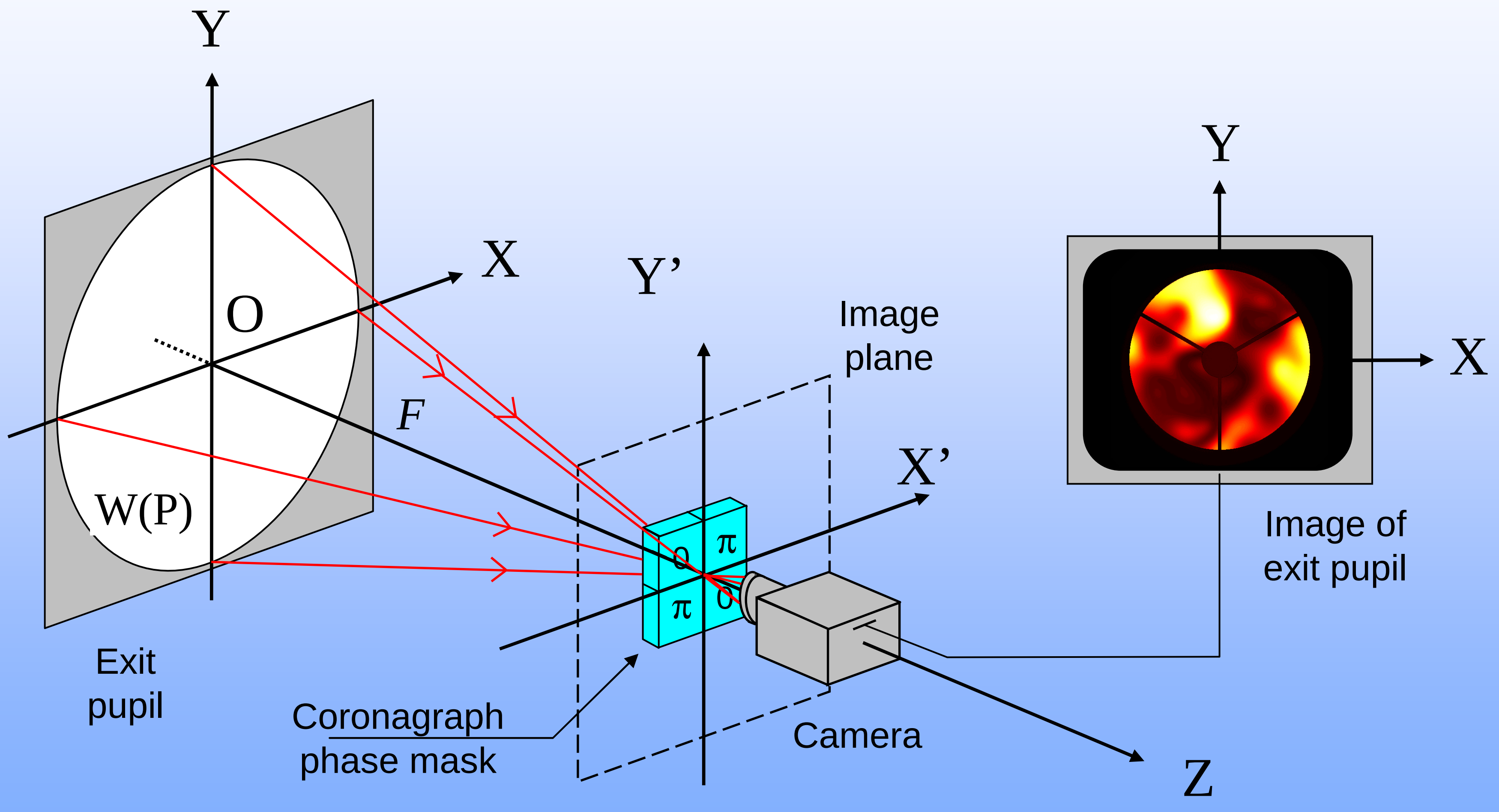

Look at pupil trough phase masks

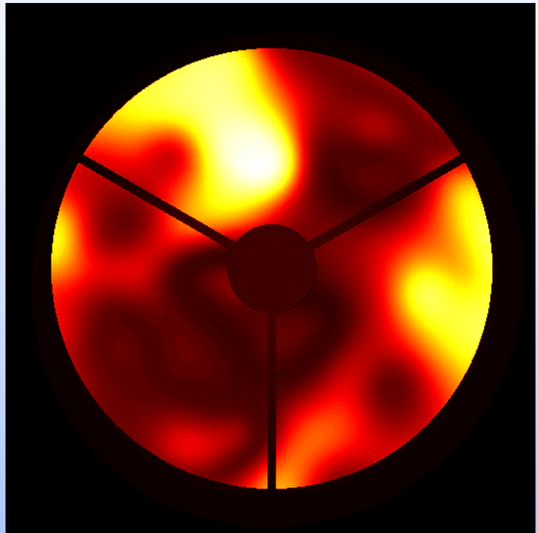

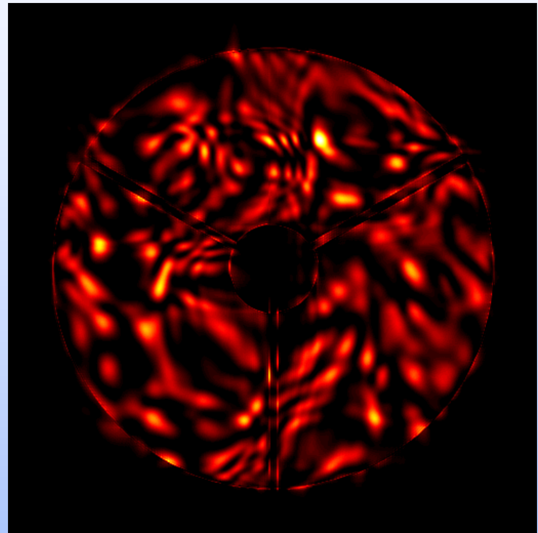

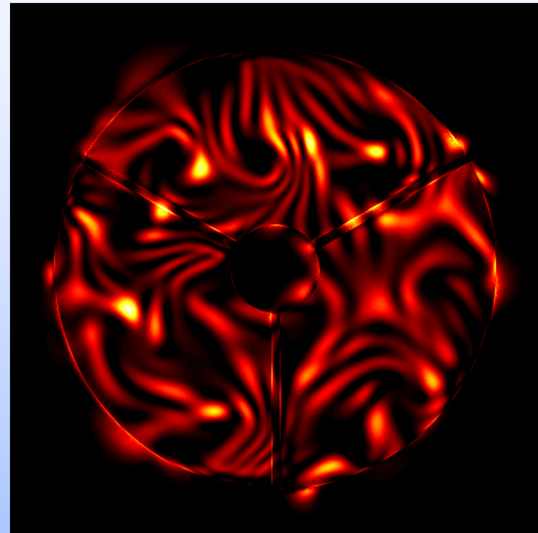

Roddier

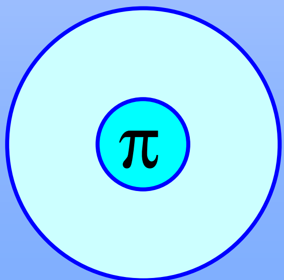

Four-Quadrant

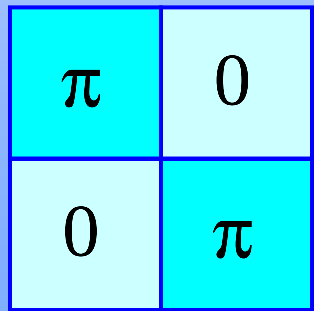

Vortex

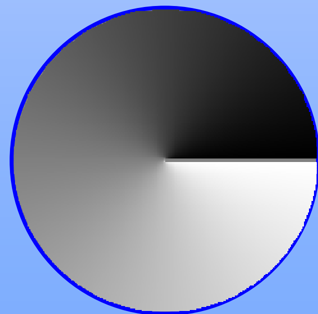

Principle

- Phase-shifting technique enables wavefront sensing behind the phase mask of a coronagraph
  - Potential reduction of Non common path aberra

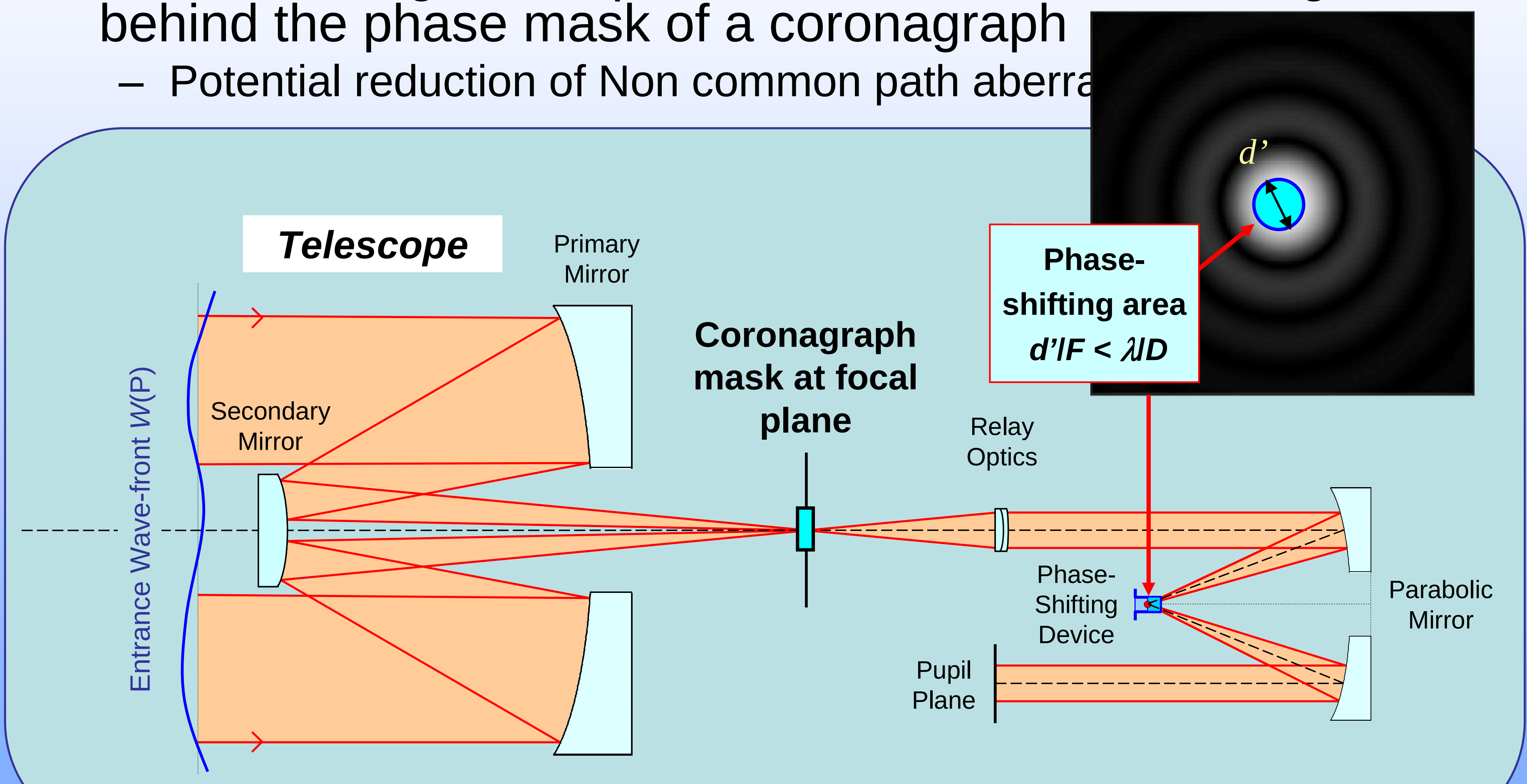

J. K. Wallace *et al*, Proc. SPIE (2011)

Measured intensities

Three sequential phase-shifts ϕ = 0, $2\pi/3$ and $4\pi/3$

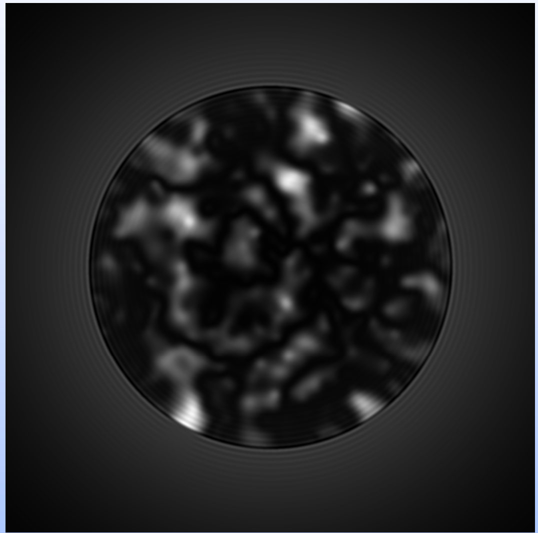

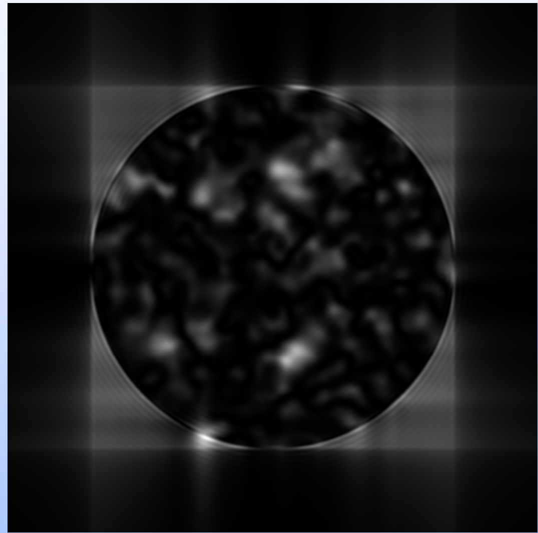

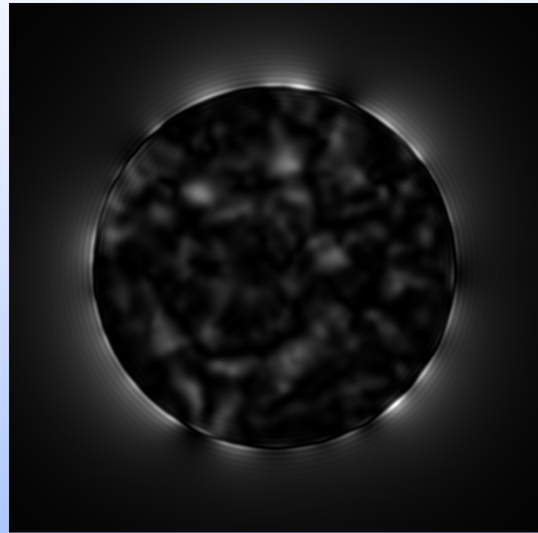

Roddier

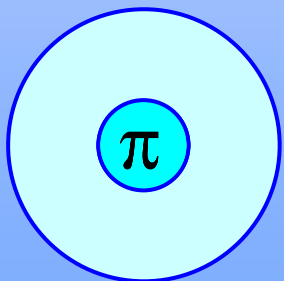

Four-Quadrant

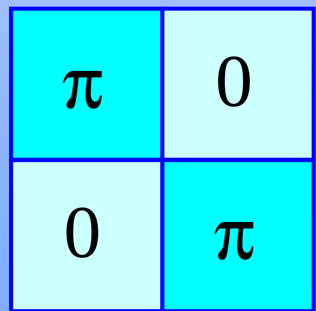

Vortex

Numerical simulations

- **1st step**: Complex amplitude propagation from plane to plane via Fourier transforms (no Fresnel diffraction)
- **2nd step**: Phase-shift reconstruction algorithm

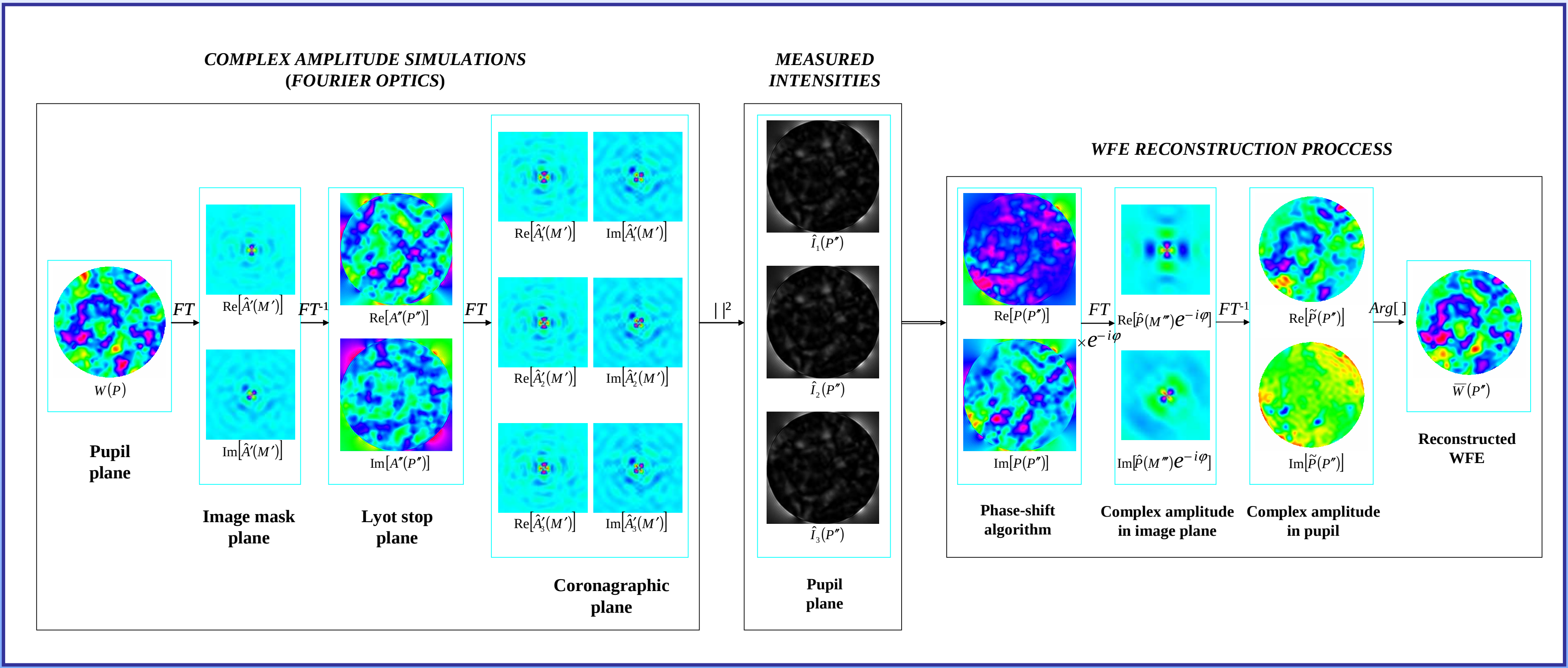

Numerical results

- Measurement accuracy is in the range **5-10 %** well below **λ/100 RMS**
  - As good as if there was no phase mask, except for the four-quadrant
  - Could operate in open loop
  - Not limited to weak aberration, but only by 2π-ambiguity

Initial WFE
PTV 0.513 λ
RMS 0.101 λ

Type of Coronagraph	***PHASE-SHIFT LOCATION***									
	Telescope pupil plane $\rho = 0.05$; $\Lambda = 4$; $0.1 < \eta < 0.9$			**Lyot stop plane** $\rho = 0.05$; $\Lambda = 4$; $0.1 < \eta < 0.9$			**Image plane** $\varepsilon = 0.1^{(*)}$; $\Lambda = 4$; $0 < \eta < 0.95$			
	Measured (waves)	Difference (waves)	Relative error (%)	Measured (waves)	Difference (waves)	Relative error (%)	Measured (waves)	Difference (waves)	Relative error (%)	
No coronagrah	0.098	0.005	5	0.098	0.005	5	0.106	0.002	2	RMS
	0.489	0.037	7	0.489	0.036	7	0.516	0.017	3	PTV
Roddier	0.107	0.008	8	0.110	0.009	9	0.104	0.007	6	RMS
	0.520	0.072	14	0.540	0.035	7	0.504	0.039	8	PTV
4-Quadrants	0.108	0.009	9	0.107	0.008	8	0.114	0.022	21	RMS
	0.519	0.079	15	0.518	0.046	9	0.542	0.080	16	PTV
Vortex (m=2)	0.101	0.004	4	0.100	0.007	7	0.110	0.006	5	RMS
	0.502	0.042	8	0.498	0.067	13	0.531	0.040	8	PTV

Numerical results – Effect of Lyot stop

- Measurement accuracy is degraded by the Lyot stop
- WFE cannot be reconstructed if the diameters *D* and D_L of the telescope pupil and Lyot stop are equal
- Best measurement accuracy achieved when $\boxed{D_L / D \geq 3}$

	Relative errors (%)			
D_L/D *ratio*	Phase-shift in Lyot stop plane		Phase-shift in coronagraph plane	
	RMS	PTV	RMS	PTV
Negative	89	85	85	85
1	*Fail*		*Fail*	
1.5	34	23	37	35
2	17	16	20	21
3	7	13	10	12
4	4	12	6	9
5	3	12	5	8
6	2	11	5	8
7	2	11	5	7
8	2	11	4	7

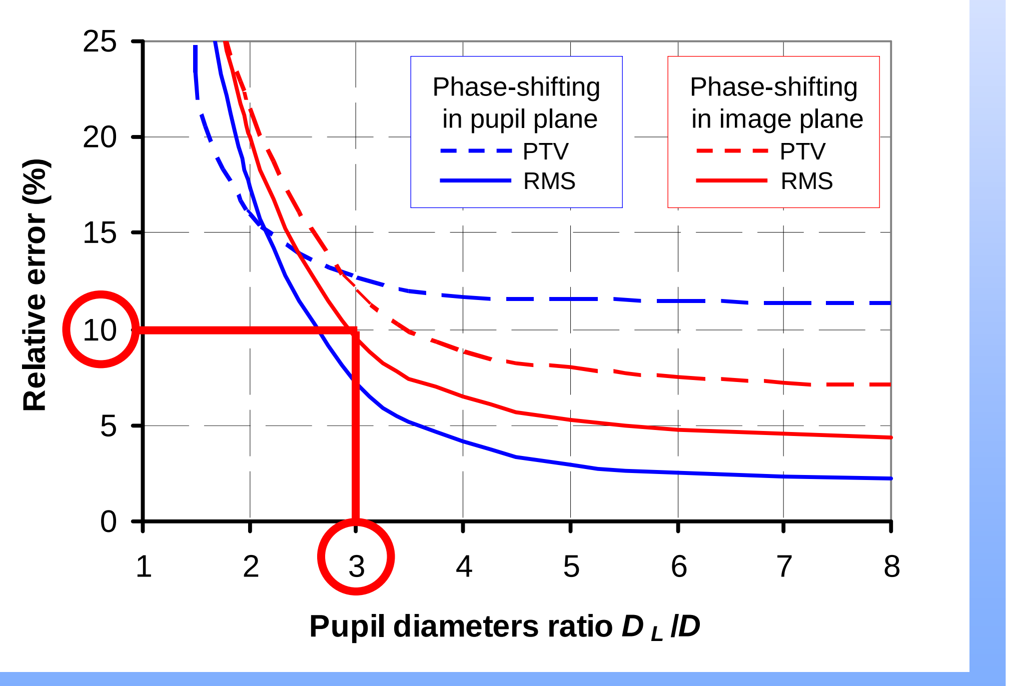

Alternative optical setup

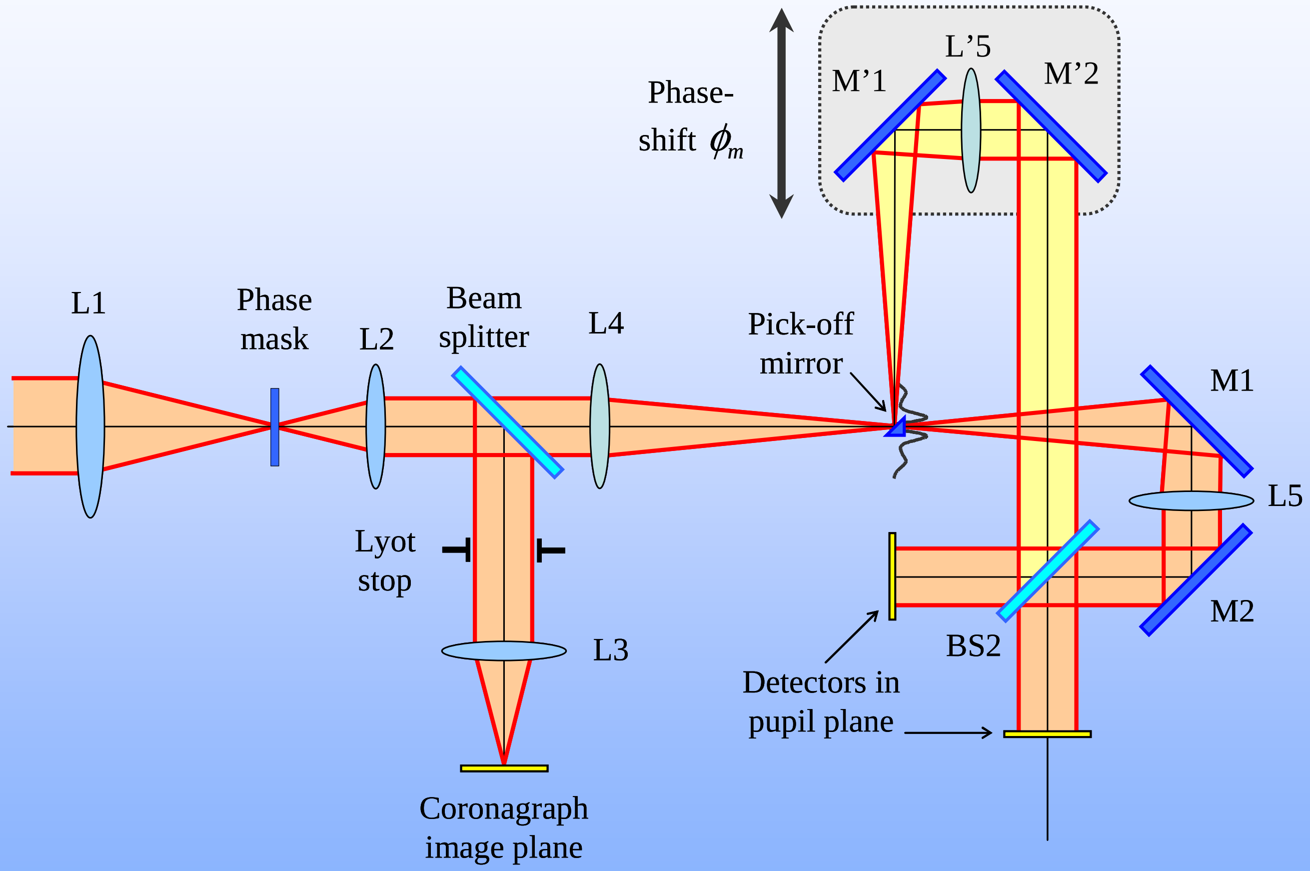

– Other solutions to be investigated: "Dichroic" Lyot stop ? Integral field spectrograph ?

A “backward gazing” solar wavefront sensor

Collaboration with PROMES lab.
Four solaire d’Odeillo, UPR CNRS-INSIS
(since 2014)

Solar concentrating facilities

(Odeillo & Targassonne, Pyrénées-Orientales, France)

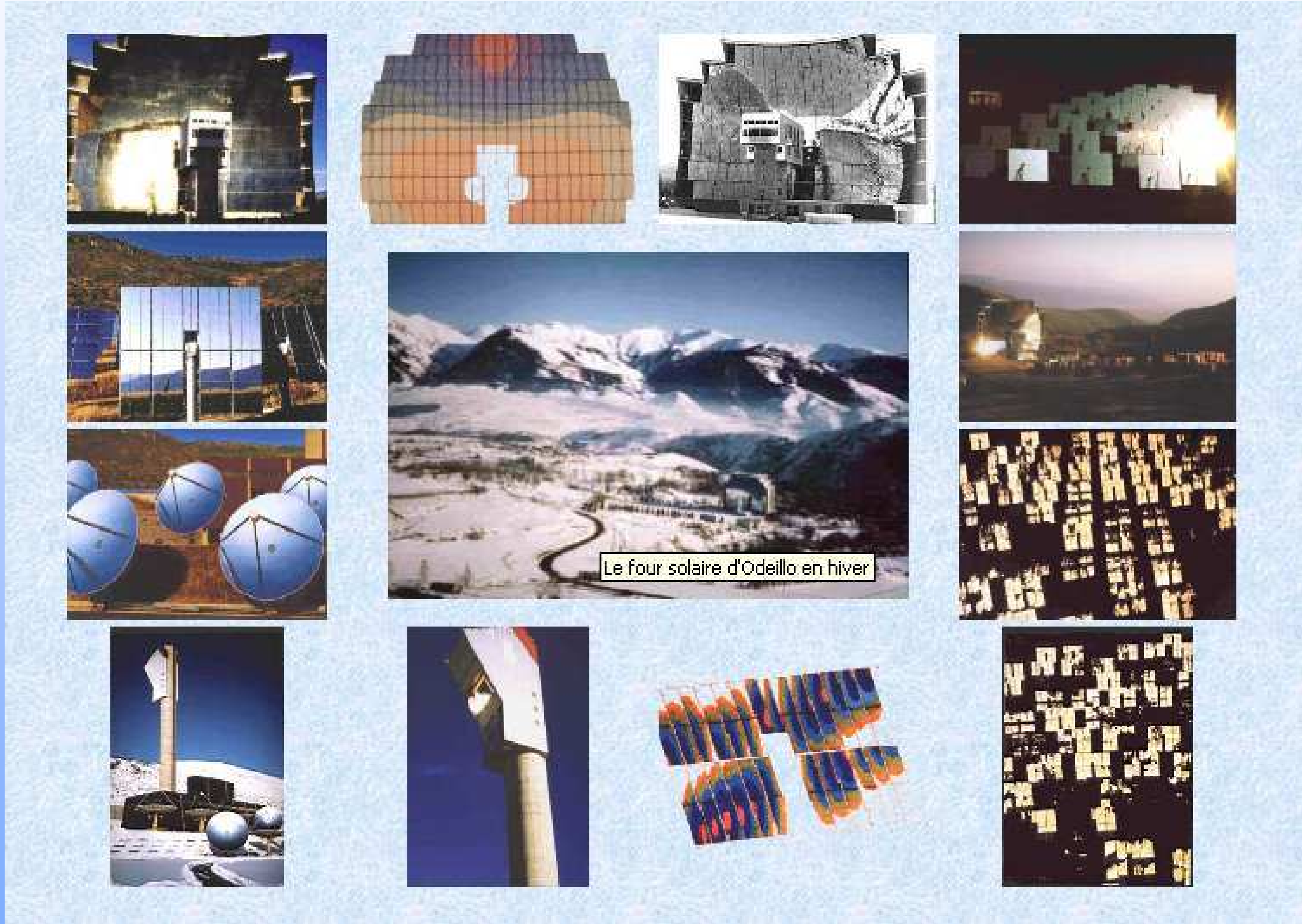

Recent experiment at THEMIS power plant

Four cameras looking at the same heliostat

Calibration camera

A 5th camera is used to calibrating the sun profile L(ε) during images acquisition

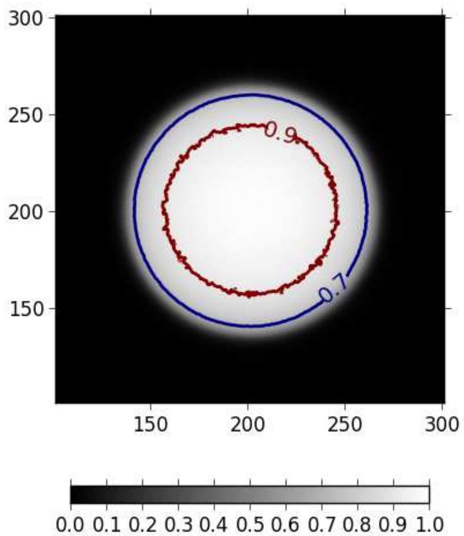

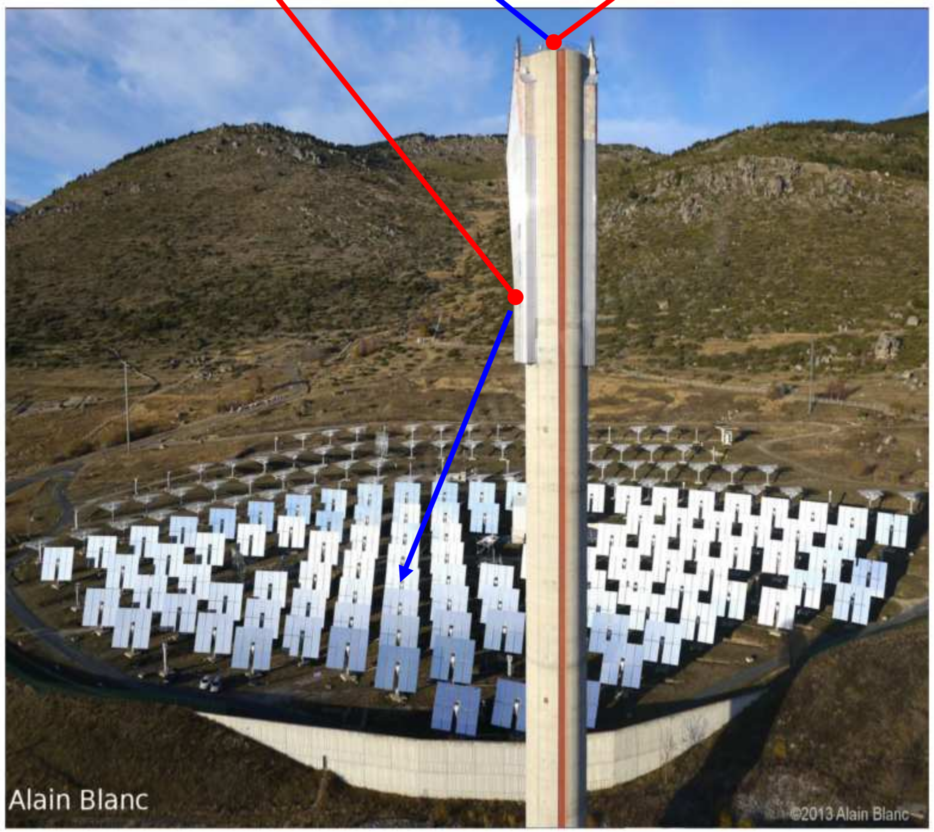

M. Coquand, C. Caliot & F. Hénault, Proceedings of the SPIE (2017)

Principle (1/3)

- Four cameras simultaneously observing sunrays through a solar concentrating mirror

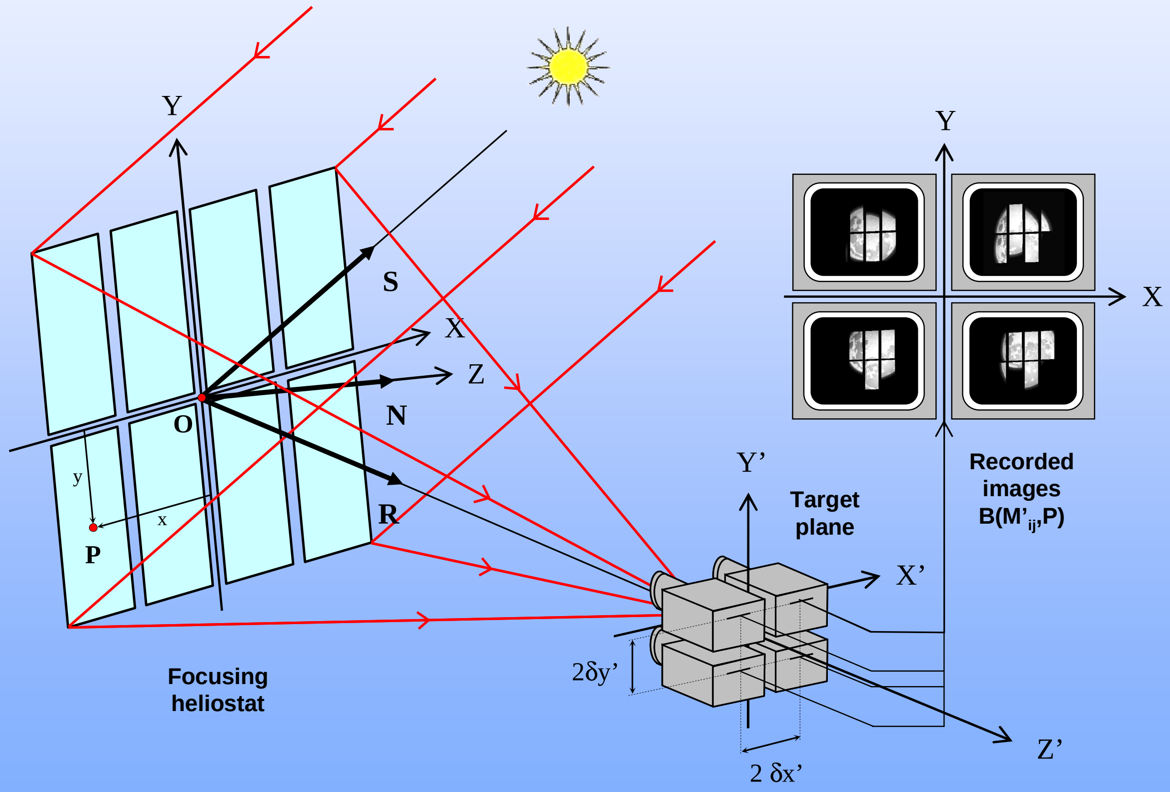

M. Coquand, F. Hénault & C. Caliot, Applied Optics (2017)

Principle (2/3)

- **1st step**: Reconstructing wavefront slopes from the acquired images and knowledge of the angular brightness function of the Sun L(ε)

$$\begin{pmatrix} \dfrac{\partial W(P)}{\partial x} \\ \dfrac{\partial W(P)}{\partial y} \end{pmatrix} = D \begin{pmatrix} \dfrac{K_{22}(P)+K_{21}(P)-K_{12}(P)-K_{11}(P)}{8\delta x'} \\ \dfrac{K_{22}(P)-K_{21}(P)+K_{12}(P)-K_{11}(P)}{8\delta y'} \end{pmatrix}$$

Generalized 4-quadrants formulas based on square inverse function of L(ε) $K(P)=\left[L^{-1}(\varepsilon(P))\right]^2$

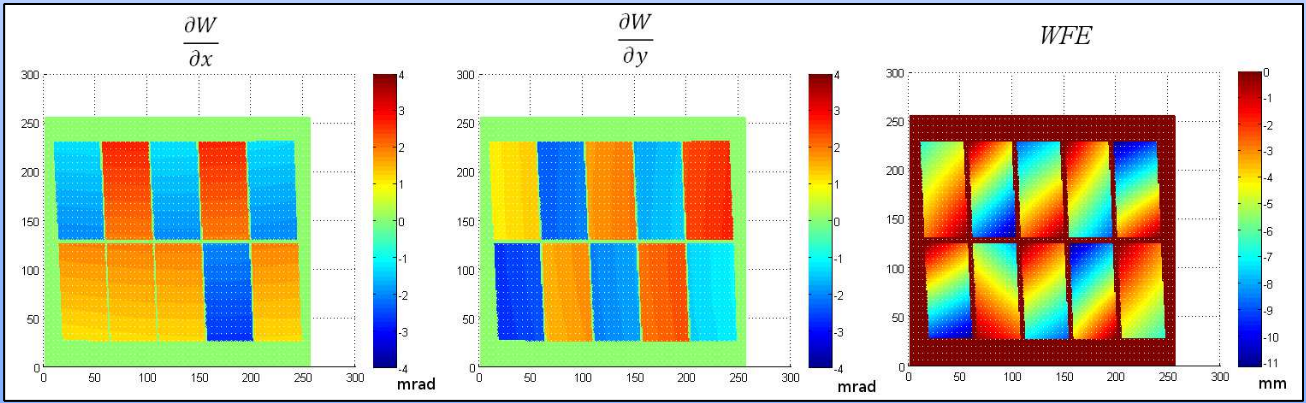

Measurement accuracy < 0.01 mrad

M. Coquand, F. Hénault & C. Caliot, Applied Optics (2017)

Principle (3/3)

- **2nd step**: Transforming wavefront slopes into actual mirror slopes

$$\begin{pmatrix} \dfrac{\partial \Delta(M)}{\partial x} \\ \dfrac{\partial \Delta(M)}{\partial y} \end{pmatrix} = \frac{1}{2} \begin{bmatrix} \dfrac{1}{\cos H} & -\tan A \tan H \\ 0 & \dfrac{1}{\cos A} \end{bmatrix} \begin{pmatrix} \dfrac{\partial W(P)}{\partial x} \\ \dfrac{\partial W(P)}{\partial y} \end{pmatrix}$$

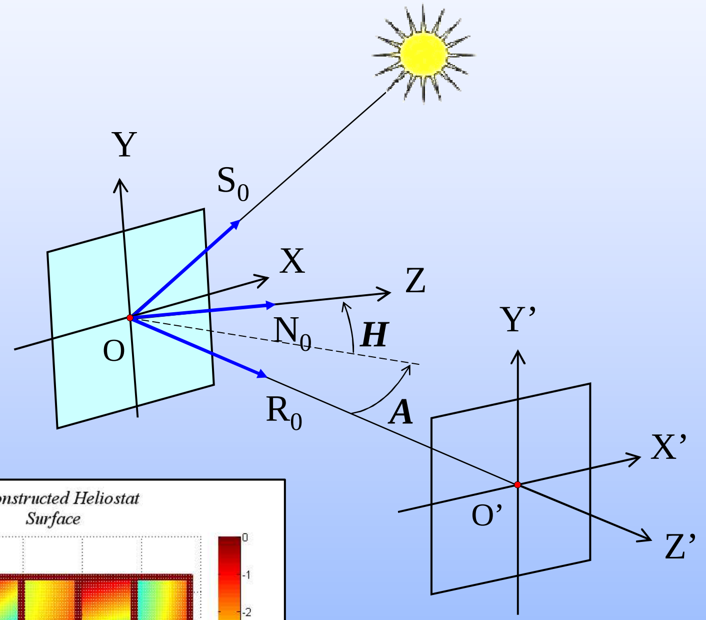

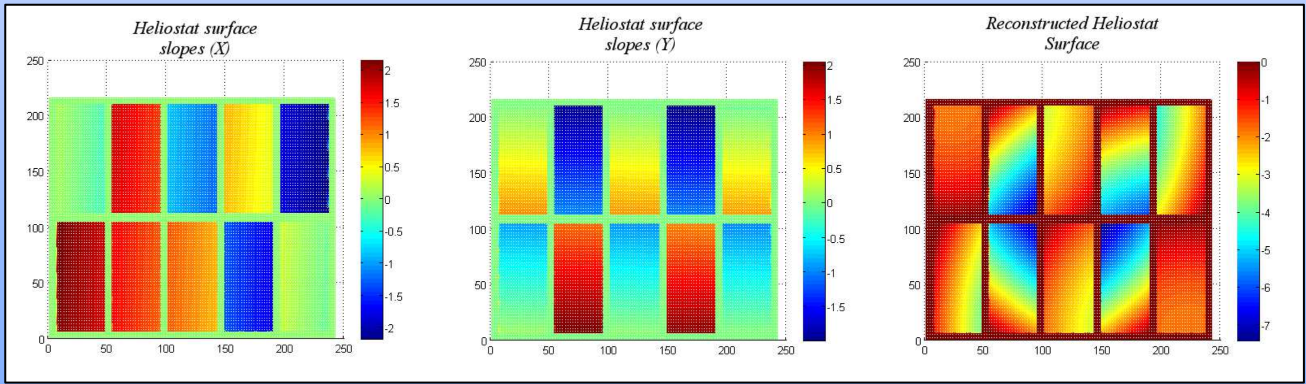

Measurement accuracy ~ 0.04 mrad

M. Coquand, F. Hénault & C. Caliot, Applied Optics (2017)

Preliminary results

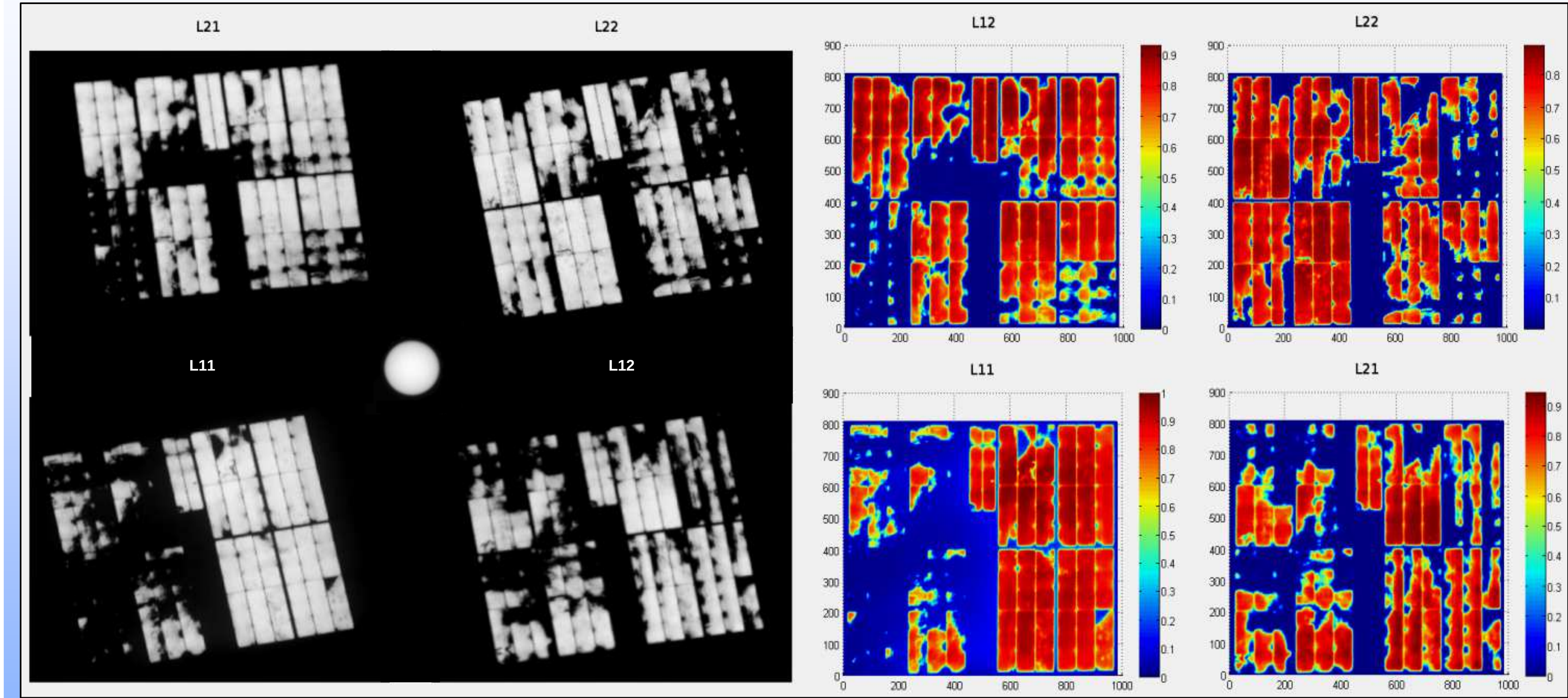

Raw images

Registered images

M. Coquand, C. Caliot & F. Hénault, Proceedings of the SPIE (2017)

Preliminary results

Mirror slopes along X-axis

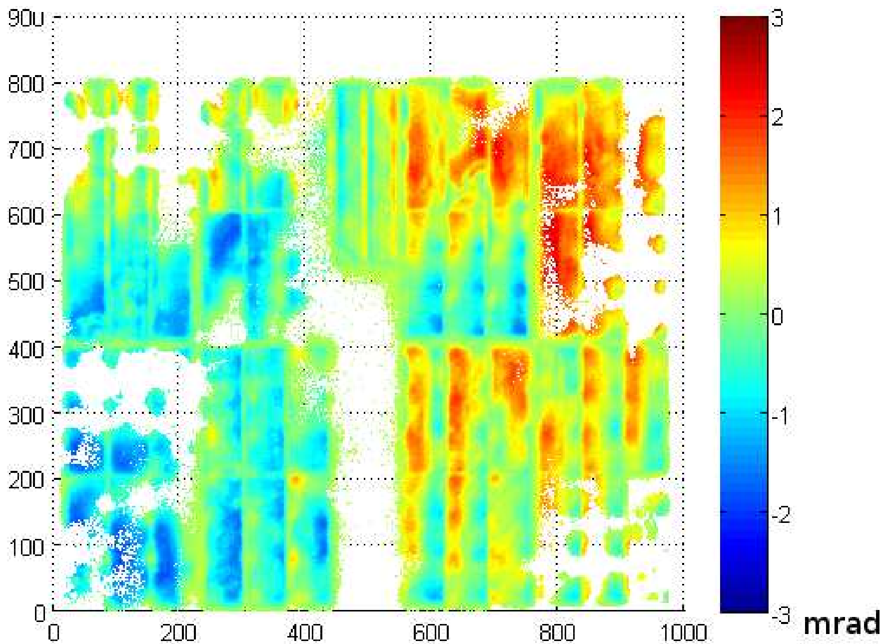

Mirror slopes along Y-axis

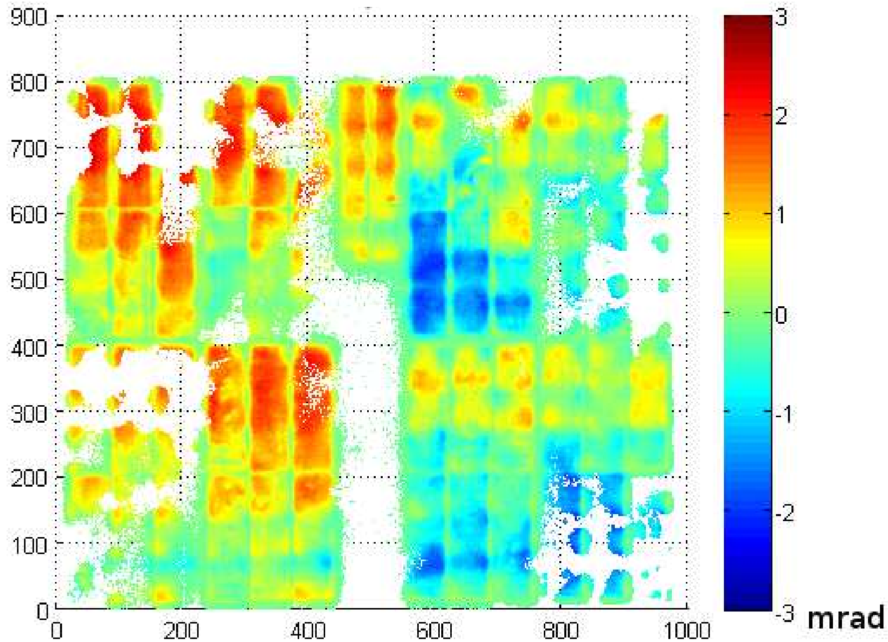

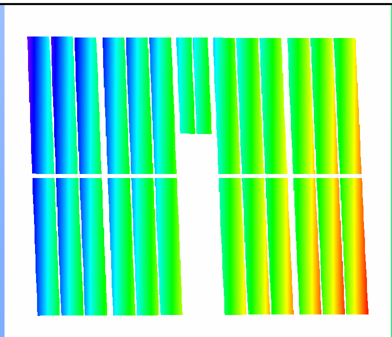

To be compared with an error free mirror

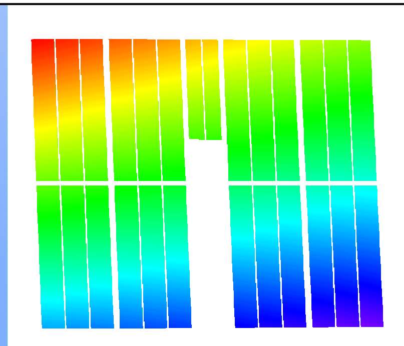

Let's conclude with a few philosophical thoughts

- With so many different types of wavefront sensors, we probably need a comparative study to find "**The Best**" (trade off). But many different parameters should be handled:
  - Type of light sources (NGS/LGS), nature of corrected perturbations (active/adaptive optics), measured quantities (WFE or its slopes), open/closed loop, use of a coronagraph, detectors characteristics and performance, etc.

→ Is a trade off still feasible ?

- Moreover, some numerical models may become excessively time-consuming, especially when dealing with extended spectral range and light sources (laser guide stars) → Brute force computing still relevant ?
- Anyway, **never** listen to people claiming "**We don't need new wavefront sensors**". We still need "better, faster, cheaper" WFS


Thank you Marseille !
Questions ?
Stade Vélodrome 26/06/2018